



ATLAS CONF Note

ATLAS-CONF-2019-040

10th August 2019



Search for squarks and gluinos in final states with jets and missing transverse momentum using 139 fb^{-1} of $\sqrt{s} = 13 \text{ TeV}$ pp collision data with the ATLAS detector

The ATLAS Collaboration

A search for the supersymmetric partners of quarks and gluons (squarks and gluinos) in final states containing jets and missing transverse momentum, but no electrons or muons, is presented. The data used in this search were recorded by the ATLAS experiment in proton–proton collisions at a center-of-mass energy of $\sqrt{s} = 13 \text{ TeV}$ during Run 2 of the Large Hadron Collider, corresponding to an integrated luminosity of 139 fb^{-1} . The results are interpreted in the context of various R -parity-conserving models where squarks and gluinos are pair-produced and a neutralino is the lightest supersymmetric particle. An exclusion limit at the 95% confidence level on the mass of the gluino is set at 2.35 TeV for a simplified model considering only a gluino and the lightest neutralino, assuming the lightest neutralino is massless. For a simplified model involving the strong production of mass-degenerate first- and second-generation squarks, squark masses below 1.94 TeV are excluded if the lightest neutralino is massless. These limits substantially extend the region of supersymmetric parameter space previously excluded by similar searches with the ATLAS detector.

1 Introduction

Supersymmetry (SUSY) [1–6] is a generalization of space-time symmetries that predicts new bosonic partners for the fermions and new fermionic partners for the bosons of the Standard Model (SM). If R -parity is conserved [7], supersymmetric particles (sparticles), are produced in pairs and the lightest supersymmetric particle (LSP) is stable and represents a possible dark-matter candidate [8, 9]. The scalar partners of the left- and right-handed quarks, the squarks \tilde{q}_L and \tilde{q}_R , mix to form two mass eigenstates \tilde{q}_1 and \tilde{q}_2 ordered by increasing mass. Superpartners of the charged and neutral electroweak and Higgs bosons also mix, producing charginos ($\tilde{\chi}^\pm$) and neutralinos ($\tilde{\chi}^0$). Squarks and the fermionic partners of the gluons, the gluinos (\tilde{g}), could be produced in strong-interaction processes at the Large Hadron Collider (LHC) [10] and decay via cascades ending with the stable LSP, which escapes the detector unseen, producing substantial missing transverse momentum (E_T^{miss}).

The large cross-sections predicted for the strong production of supersymmetric particles make the gluinos and squarks a primary target in searches for SUSY in proton–proton (pp) collisions at a center-of-mass energy of 13 TeV at the LHC. Interest in these searches comes from the large available choice of parameters for R -parity-conserving models in the Minimal Supersymmetric Standard Model (MSSM) [11, 12] where squarks (including anti-squarks) and gluinos can be produced in pairs ($\tilde{g}\tilde{g}$, $\tilde{q}\tilde{q}$, $\tilde{q}\tilde{g}$) and can decay through $\tilde{q} \rightarrow q\tilde{\chi}_1^0$ and $\tilde{g} \rightarrow qq\tilde{\chi}_1^0$ to the lightest neutralino, $\tilde{\chi}_1^0$, assumed to be the LSP. Additional decay modes can include the production of charginos via $\tilde{q} \rightarrow q'\tilde{\chi}^\pm$ (where \tilde{q} and q' are of different flavor) and $\tilde{g} \rightarrow qq'\tilde{\chi}^\pm$. Subsequent chargino decays to $W^\pm\tilde{\chi}_1^0$, depending on the decay modes of the W bosons, can increase the jet multiplicity and missing transverse momentum in these events.

This document presents a search for these sparticles, using two approaches, in final states containing exclusively hadronic jets and large missing transverse momentum. The first, referred to as the ‘multi-bin search’, extends the previous search from Ref. [13] by simultaneously fitting multiple bins. The second, referred to as the ‘BDT search’, is a complementary search which uses boosted decision trees (BDTs) implemented in the TMVA framework [14] for the event selection. The BDT search improves the sensitivity to supersymmetric models where gluinos decay via an intermediate chargino because of its highly optimized design and ability to exploit the correlations between variables. The CMS Collaboration has set limits on similar models in Refs. [15–20].

In the searches presented here, events with reconstructed electrons or muons are rejected to reduce the background from events with neutrinos ($W \rightarrow e\nu, \mu\nu$) and to avoid any overlap with a complementary ATLAS search in final states with one lepton, jets and missing transverse momentum [21]. The selection criteria are optimized in the $(m(\tilde{g}), m(\tilde{\chi}_1^0))$ and $(m(\tilde{q}), m(\tilde{\chi}_1^0))$ planes, (where $m(\tilde{g})$, $m(\tilde{q})$ and $m(\tilde{\chi}_1^0)$ are the gluino, squark and the LSP masses, respectively) for simplified models [22–24] in which all other supersymmetric particles are assigned masses beyond the reach of the LHC. Although interpreted in terms of SUSY models, the results of this analysis can also constrain any model of new physics that predicts the production of jets in association with missing transverse momentum.

The document is organized as follows. Section 2 describes the ATLAS experiment and the data sample used for the search, and Section 3 the Monte Carlo (MC) simulation samples used for background and signal modelling. The physics object reconstruction and identification are presented in Section 4. The searches are performed in signal regions which are defined in Section 5. Summaries of the background estimation methodology and corresponding systematic uncertainties are presented in Sections 6 and 7, respectively. Results obtained for both searches are reported in Section 8. Section 9 is devoted to a summary and conclusions.

2 The ATLAS detector and data samples

The ATLAS detector [25] is a multipurpose detector with a forward-backward symmetric cylindrical geometry and nearly 4π coverage in solid angle.¹ The inner detector (ID) tracking system consists of pixel and silicon microstrip detectors covering the pseudorapidity region $|\eta| < 2.5$, surrounded by a transition radiation tracker, which improves electron identification over the region $|\eta| < 2.0$. The innermost pixel layer, the insertable B-layer [26, 27], was added between Run 1 and Run 2 of the LHC, at a radius of 33 mm around a new, narrower and thinner beam pipe. The ID is surrounded by a thin superconducting solenoid providing an axial 2 T magnetic field and by a fine-granularity lead/liquid-argon (LAr) electromagnetic calorimeter covering $|\eta| < 3.2$. A steel/scintillator-tile calorimeter provides hadronic coverage in the central pseudorapidity range ($|\eta| < 1.7$). The endcap and forward calorimeters ($1.5 < |\eta| < 4.9$) are made of LAr active layers with either copper or tungsten as the absorber material for electromagnetic and hadronic measurements. The muon spectrometer with an air-core toroid magnet system surrounds the calorimeters. Three layers of high-precision tracking chambers provide coverage in the range $|\eta| < 2.7$, while dedicated chambers allow triggering in the region $|\eta| < 2.4$.

The ATLAS trigger system [28] consists of two levels; the first level is a hardware-based system, while the second is a software-based system called the high-level trigger. The events used by the searches described in this paper were selected using a trigger logic that accepts events with a missing transverse momentum above 70–110 GeV, depending on the data-taking period. The trigger is approximately 100% efficient for the event selections considered in these searches. Auxiliary data samples used to estimate or validate the yields of $Z(\rightarrow \nu\bar{\nu})$ +jets background events were selected using triggers requiring at least one isolated photon ($p_T > 120$ GeV), electron ($p_T > 24$ GeV) or muon ($p_T > 20$ GeV), for data collected in 2015. For the 2016–2018 data, these events were selected using triggers requiring at least one isolated electron or muon ($p_T > 26$ GeV) or photon ($p_T > 140$ GeV).

The data were collected by the ATLAS detector during 2015–2018 with a center-of-mass energy of 13 TeV and a 25 ns proton bunch crossing interval. In 2015–2016 the average number of pp interactions per bunch crossing (pile-up) was $\langle\mu\rangle = 20$ increasing to $\langle\mu\rangle = 38$ in 2017 and to $\langle\mu\rangle = 37$ in 2018. Application of beam, detector and data-quality criteria resulted in a total integrated luminosity of 139 fb^{-1} . The uncertainty in the combined 2015–2018 integrated luminosity is 1.7% [29], obtained using the LUCID-2 detector [30] for the primary luminosity measurements.

3 Simulated event samples

A common set of simulated Monte Carlo (MC) data samples is used by both searches presented in this document to optimize the selections, aid the estimation of backgrounds and assess the sensitivity to specific SUSY signal models.

¹ ATLAS uses a right-handed coordinate system with its origin at the nominal interaction point in the center of the detector. The positive x -axis is defined by the direction from the interaction point to the center of the LHC ring, with the positive y -axis pointing upwards, while the beam direction defines the z -axis. Cylindrical coordinates (r, ϕ) are used in the transverse plane, ϕ being the azimuthal angle around the z -axis. The pseudorapidity η is defined in terms of the polar angle θ by $\eta = -\ln \tan(\theta/2)$ and the rapidity is defined as $y = (1/2) \ln[(E + p_z)/(E - p_z)]$ where E is the energy and p_z the longitudinal momentum of the object of interest. The transverse momentum p_T , the transverse energy E_T and the missing transverse momentum are defined in the x – y plane unless stated otherwise.

Simplified model signal samples are used to describe the production of squarks and gluinos. The topologies considered include squark- or gluino-pair production, followed by the direct ($\tilde{q} \rightarrow q\tilde{\chi}_1^0$) or one-step ($\tilde{q} \rightarrow q'\tilde{\chi}_1^\pm \rightarrow q'W\tilde{\chi}_1^0$) decays of squarks shown in Figure 1(a, b), and direct ($\tilde{g} \rightarrow qq\tilde{\chi}_1^0$) or one-step ($\tilde{g} \rightarrow qq'\tilde{\chi}_1^\pm \rightarrow qq'W\tilde{\chi}_1^0$) decays of gluinos as shown in Figure 1(c, d), respectively. Direct decays are those where the squarks or gluinos decay directly into SM particles and the LSP, while the one-step decays refer to the cases where the decays occur via one intermediate on-shell SUSY particle. An additional simplified model scenario in which squark-pair, gluino-pair, and squark-gluino are produced inclusively is also considered. In this scenario, all production processes (gluino-gluino, squark-antisquark, squark-squark, antisquark-antisquark and squark-gluino) are included, and the produced squarks and/or gluinos can follow the direct decays indicated in Figure 1(a, c, e), or decays of squarks via gluinos ($\tilde{q} \rightarrow q\tilde{g}$) and decays of gluinos via squarks ($\tilde{g} \rightarrow q\tilde{q}$) if kinematically possible. The branching ratios for these decays are calculated with the SUSY-HIT program [31]. The free parameters are $m(\tilde{\chi}_1^0)$ and $m(\tilde{q})$ ($m(\tilde{g})$) for squark-pair (gluino-pair) production with direct decays of squark and gluinos. In the case of squark- or gluino-pair production models with one-step decays, the free parameters are $m(\tilde{q})$ or $m(\tilde{g})$, and either $m(\tilde{\chi}_1^\pm)$ (with a fixed $m(\tilde{\chi}_1^0) = 60$ GeV) or $m(\tilde{\chi}_1^0)$ (with $m(\tilde{\chi}_1^\pm) = (m(\tilde{g}/\tilde{q}) + m(\tilde{\chi}_1^0))/2$). For models with inclusive production of squarks and gluinos both $m(\tilde{q})$ and $m(\tilde{g})$ are varied with $m(\tilde{\chi}_1^0)$ fixed to 0 GeV, 995 GeV, and 1495 GeV. All other supersymmetric particles, including the squarks of the third generation, have their masses set such that the particles are effectively decoupled. Eightfold degeneracy of first- and second-generation squarks is assumed for the simplified models with direct decays of squarks, while fourfold degeneracy is assumed for the simplified models with one-step decays of squarks. The gluino is allowed to decay into four flavors (u, d, s, c) of quarks in simplified models with gluino-pair production.

These samples were generated with up to two extra partons in the matrix element using the MG5_aMC@NLO 2.6.1 event generator [32] (for signal samples describing squark- and gluino-pair production followed by the direct decay of squarks and gluinos) or MG5_aMC@NLO 2.6.2 (for signal samples describing squark-gluino production and squark- and gluino-pair production followed by the one-step decay of squarks and gluinos) interfaced to PYTHIA 8.212 and PYTHIA 8.230 [33], respectively. The CKKW-L merging scheme [34] was applied with a scale parameter that was set to a quarter of the mass of the gluino for $\tilde{g}\tilde{g}$ production or of the squark for $\tilde{q}\tilde{q}$ production in simplified models. In models with squark, gluino, and squark-gluino pairs, a quarter of the smaller of the gluino and squark masses was used for the CKKW-L merging scale. The A14 [35] set of tuned parameters (tune) was used for initial/final-state radiation (ISR/FSR) and underlying-event parameters together with the NNPDF2.3LO [36] parton distribution function (PDF) set.

Signal cross sections are calculated to approximate next-to-next-to-leading order in the strong coupling constant, adding the resummation of soft gluon emission at next-to-next-to-leading-logarithmic accuracy (approximate NNLO+NNLL) [37–44]. The nominal cross section and the uncertainty are derived using the PDF4LHC15_mc PDF set, following the recommendations of Ref. [45], considering only first- and second-generation squarks ($\tilde{u}, \tilde{d}, \tilde{s}, \tilde{c}$), except in the case of models describing squark-pair production followed by the direct decay of squarks, where five flavors ($\tilde{u}, \tilde{d}, \tilde{s}, \tilde{c}, \tilde{b}$) are considered.

A summary of all SM background processes together with the MC event generators, cross-section calculation orders in α_s , PDFs, parton shower and tunes used is given in Table 1.

For all SM background samples the response of the detector to particles was modeled with the full ATLAS detector simulation [60] based on GEANT4 [61]. Signal samples were prepared using a fast simulation based on a parameterization of the performance of the ATLAS electromagnetic and hadronic calorimeters and on GEANT4 elsewhere. The EvtGen v1.2.0 program [62] was used to describe the properties of the

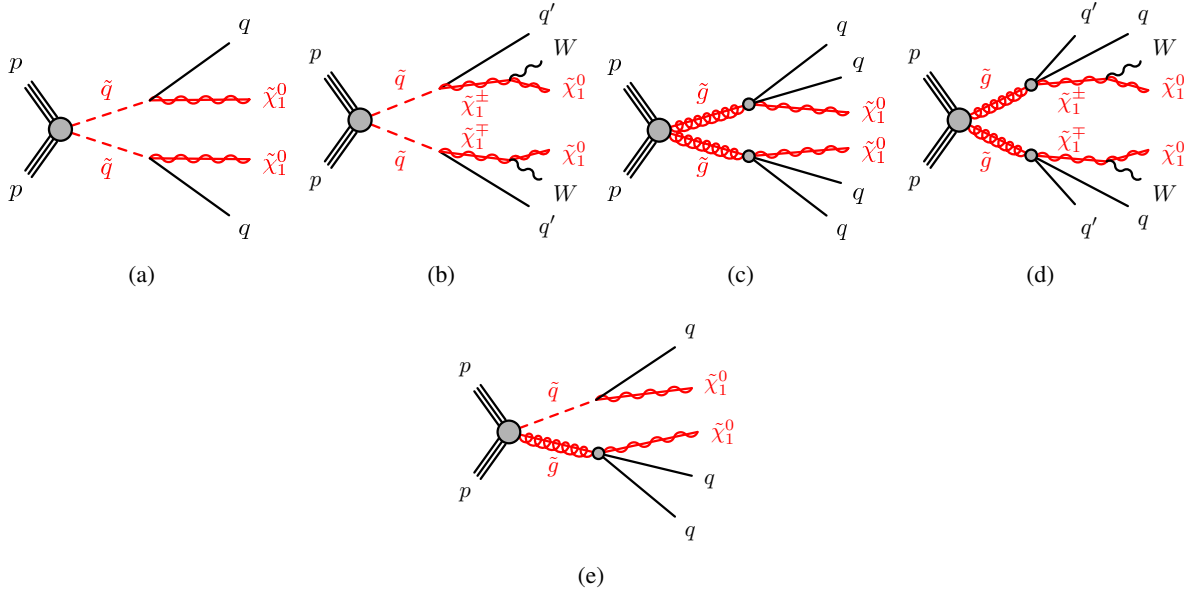


Figure 1: The decay topologies of (a, b) squark-pair production, (c, d) gluino-pair production and (e) squark-gluino production in simplified models with (a, c, e) direct decays of squarks and gluinos or (b, d) one-step decays of squarks and gluinos.

Physics process	Generator	Cross-section normalization	PDF set	Parton shower	Tune
$W(\rightarrow \ell\nu) + \text{jets}$	SHERPA 2.2.1 [46]	NNLO [47]	NNPDF3.0NNLO [48]	SHERPA [49]	SHERPA
$Z/\gamma^*(\rightarrow \ell\bar{\ell}) + \text{jets}$	SHERPA 2.2.1	NNLO	NNPDF3.0NNLO	SHERPA	SHERPA
$\gamma + \text{jets}$	SHERPA 2.2.2	NLO	NNPDF3.0NNLO	SHERPA	SHERPA
$t\bar{t}$	POWHEG-BOX v2 [50]	NNLO+NNLL [51, 52]	NNPDF2.3LO [36]	PYTHIA 8.230 [33]	A14 [53]
Single top (Wt -channel)	POWHEG-BOX v2	NNLO+NNLL [54, 55]	NNPDF2.3LO	PYTHIA 8.230	A14
Single top (s -channel)	POWHEG-BOX v2	NLO [56, 57]	NNPDF2.3LO	PYTHIA 8.230	A14
Single top (t -channel)	POWHEG-BOX v1	NLO	NNPDF2.3LO	PYTHIA 8.230	A14
$t\bar{t} + W/Z/H$	MG5_aMC@NLO 2.2.3 [32]	NLO [58, 59]	NNPDF2.3LO	PYTHIA 8.210	A14
$t\bar{t} + WW$	MG5_aMC@NLO 2.2.2	NLO	NNPDF2.3LO	PYTHIA 8.210	A14
$WW, WZ, ZZ, W\gamma, Z\gamma$	SHERPA 2.2.1	NLO	NNPDF3.0NNLO	SHERPA	SHERPA

Table 1: The SM background MC simulation samples used in this paper. The generators, the order in α_s of cross-section calculations used for yield normalization, PDF sets, parton showers and tunes used for the underlying event are shown.

b- and *c*-hadron decays in the signal samples, and the background samples except those produced with SHERPA [46].

All simulated events were overlaid with multiple pp collisions simulated with PYTHIA 8.186 using the A3 tune [35] and the NNPDF2.3LO parton distribution functions [36]. The MC samples were generated with a variable number of additional pp interactions (pileup), and were reweighted to match the distribution of the mean number of interactions observed in data in 2015–2018.

4 Object reconstruction and identification

The reconstructed primary vertex of the event is required to be consistent with the luminous region and to have at least two associated tracks with $p_T > 500$ MeV. When more than one such vertex is found, the vertex with the largest $\sum p_T^2$ of the associated tracks is chosen.

Jet candidates are reconstructed using the anti- k_t jet clustering algorithm [63, 64] with a jet radius parameter of 0.4 starting from clusters of calorimeter cells [65]. The jets are corrected for energy from pileup using the method described in Ref. [66]: a contribution equal to the product of the jet area and the median energy density of the event is subtracted from the jet energy [67]. Further corrections, referred to as the jet energy scale corrections, are derived from MC simulation and data, and are used to calibrate the average energies of jets to the scale of their constituent particles [68]. Only corrected jet candidates with $p_T > 20$ GeV and $|\eta| < 2.8$ are retained. An algorithm based on boosted decision trees, ‘MV2c10’ [69, 70], is used to identify jets containing a b -hadron (b -jets), with an operating point corresponding to an efficiency of 77%, and rejection factors of about 130 for jets originating from gluons and light-flavour quarks (light jets) and about 6 for jets induced by charm quarks. Candidate b -jets are required to have $p_T > 50$ GeV and $|\eta| < 2.5$. Events with jets originating from detector noise and non-collision background are rejected if the jets fail to satisfy the ‘LooseBad’ quality criteria, or if at least one of the two leading jets fails to satisfy the ‘TightBad’ quality criteria, both described in Ref. [71]. The application of these requirements reduces the data sample by $\sim 9\%$. In order to reduce the number of jets coming from pileup, a significant fraction of the tracks associated with each jet must have an origin compatible with the primary vertex. This is enforced by using the jet vertex tagger (JVT) output using the momentum fraction of tracks [72]. The requirement $\text{JVT} > 0.59$ is only applied to jets with $p_T < 120$ GeV and $|\eta| < 2.5$, while in the region $2.4 < |\eta| < 2.5$, a looser value, $\text{JVT} > 0.11$ is used.

Two different classes of reconstructed lepton candidates (electrons or muons) are used in the analyses presented here. When selecting samples for the search, events containing a ‘baseline’ electron or muon are rejected. The selections applied to identify baseline leptons are designed to maximize the efficiency with which W +jets and top quark background events are rejected. When selecting events for the purpose of estimating residual W +jets and top quark backgrounds, additional requirements are applied to leptons to ensure greater purity of these backgrounds. These leptons are referred to as ‘high-purity’ leptons below and form a subset of the baseline leptons.

Baseline muon candidates are formed by combining information from the muon spectrometer and inner detector as described in Ref. [73] and are required to have $p_T > 6$ GeV and $|\eta| < 2.7$. High-purity muon candidates must additionally have the significance of the transverse impact parameter with respect to the primary vertex $|d_0^{\text{PV}}|/\sigma(d_0^{\text{PV}}) < 3$, and the longitudinal impact parameter with respect to the primary vertex $|z_0^{\text{PV}} \sin(\theta)| < 0.5$ mm. Furthermore, high-purity candidates must satisfy the ‘FCTight’ isolation requirements described in Ref. [73], which rely on tracking- and calorimeter-based variables and implement a set of η - and p_T -dependent criteria.

Baseline electron candidates are reconstructed from an isolated electromagnetic calorimeter energy deposit matched to an ID track and are required to have $p_T > 7$ GeV, $|\eta| < 2.47$, and to satisfy ‘Loose’ likelihood-based identification criteria described in Ref. [74]. High-purity electron candidates additionally must satisfy ‘Tight’ selection criteria described in Ref. [74]. They are also required to have $|d_0^{\text{PV}}|/\sigma(d_0^{\text{PV}}) < 5$, $|z_0^{\text{PV}} \sin(\theta)| < 0.5$ mm, and to satisfy isolation requirements similar to those applied to high-purity muons [75].

After the selections described above, ambiguities between electrons and muons are resolved to avoid double counting and/or remove non-isolated leptons: the electron is discarded if a baseline electron and a baseline muon share the same ID track. Ambiguities between candidate jets with $|\eta| < 2.8$ and leptons are resolved as follows: first, any such jet candidate lying within a distance $\Delta R \equiv \sqrt{(\Delta y)^2 + (\Delta\phi)^2} = 0.2$ of a baseline electron is discarded. Additionally, if a baseline electron or muon and a jet are found within $\Delta R < \min(0.4, 0.04 + 10 \text{ GeV}/p_T^{e/\mu})$, it is interpreted as a jet and the nearby electron or muon candidate is discarded. Finally, if a baseline muon and jet are found within $\Delta R < 0.2$, and jet satisfies $N_{\text{trk}} < 3$ (where N_{trk} refers to the number of tracks with $p_T > 500 \text{ MeV}$ that are associated with the jet), it is treated as a muon and the overlapping jet is ignored. This criterion rejects jets consistent with final-state radiation or hard bremsstrahlung.

Reconstructed photons are used in the missing transverse momentum reconstruction as well as in the control region used to constrain the $Z+\text{jets}$ background, as explained in Section 6. These photon candidates are required to satisfy $p_T > 25 \text{ GeV}$ and $|\eta| < 2.37$, excluding the transition region $1.37 < |\eta| < 1.52$ between the barrel and endcap EM calorimeters, photon shower shape and electron rejection criteria, and to be isolated [76]. The reduced η range for photons is chosen to avoid a region of coarse granularity at high η where photon and π^0 separation worsens. Ambiguities between candidate jets and photons (when used in the event selection) are resolved by discarding any jet candidates lying within $\Delta R = 0.4$ of a photon candidate. Additional selections to remove ambiguities between electrons or muons and photons are applied such that a photon is discarded if it is within $\Delta R = 0.4$ of a baseline electron or muon.

The measurement of the missing transverse momentum vector $\mathbf{p}_T^{\text{miss}}$ (and its magnitude E_T^{miss}) is based on the calibrated transverse momenta of all electron, muon, jet candidates, photons and all tracks originating from the primary vertex and that are not associated with the preceding reconstructed objects [77, 78].

Corrections derived from data control samples are applied to account for differences between data and simulation for the lepton and photon trigger and reconstruction efficiencies, the lepton momentum/energy scale and resolution, jet vertex tagger, and for the efficiency and mis-tag rate of the b -tagging algorithm.

5 Event selection and signal regions definitions

Due to the high mass scale expected for the SUSY models considered in this study, the ‘effective mass’, m_{eff} , defined to be the scalar sum of E_T^{miss} and the transverse momenta of all jets with $p_T > 50 \text{ GeV}$, is a powerful discriminant between the signal and most SM backgrounds. In some regions, when selecting events with at least N_j jets, $m_{\text{eff}}(N_j)$ is calculated using the transverse momenta of the leading N_j jets with $p_T > 50 \text{ GeV}$ and E_T^{miss} . Only jets with $p_T > 50 \text{ GeV}$ are used to select events in the searches presented in this document.

Following the event reconstruction described in Section 4, a common set of preselection criteria is used in the searches. Events are discarded if a baseline electron (muon) with $p_T > 7$ (6) GeV remains after resolving the ambiguities between the objects, or if they contain a jet failing to satisfy quality selection criteria designed to suppress detector noise and non-collision backgrounds (described in Section 4). Events are also rejected if no second jet with $p_T > 50 \text{ GeV}$ is found, the leading jet p_T is smaller than 200 GeV , the missing transverse momentum in the event is smaller than 300 GeV , or the effective mass is smaller than 800 GeV . In addition, the selection requires the smallest azimuthal separation between the $\mathbf{p}_T^{\text{miss}}$ and the momenta of up to three leading jets, $\Delta\phi(j_{1,2,(3)}, \mathbf{p}_T^{\text{miss}})_{\text{min}} > 0.4$. A summary of these preselection criteria

is given in Table 2. The remaining events are then analyzed in two complementary searches, both of which require the presence of jets and significant missing transverse momentum.

Lepton veto	No baseline electron (muon) with $p_T > 7$ (6) GeV
E_T^{miss} [GeV]	> 300
$p_T(j_1)$ [GeV]	> 200
$p_T(j_2)$ [GeV]	> 50
$\Delta\phi(j_{1,2,(3)}, \mathbf{p}_T^{\text{miss}})_{\text{min}}$ [rad.]	> 0.4
m_{eff} [GeV]	> 800

Table 2: Summary of common preselection criteria used for the searches presented in this document.

To search for a possible signal, selection criteria are defined to enhance the expected signal yield relative to the SM backgrounds. Signal regions (SRs) are defined using the MC simulation of SUSY signals and the SM background processes. The SRs are optimized to maximize the expected discovery sensitivity for each signal model considered. In order to maximize the sensitivity in the $m(\tilde{g}), m(\tilde{q})$ plane, a variety of signal regions are defined. Squarks typically generate at least one jet in their decays, for instance through $\tilde{q} \rightarrow q\tilde{\chi}_1^0$, while gluinos typically generate at least two jets, for instance through $\tilde{g} \rightarrow qq\tilde{\chi}_1^0$. Processes contributing to $\tilde{q}\tilde{q}$ and $\tilde{g}\tilde{g}$ final states therefore lead to events containing at least two or four jets, respectively. Decays of heavy SUSY and SM particles produced in longer \tilde{q} and \tilde{g} decay cascades tend to further increase the jet multiplicity in the final state. To target different sparticle production scenarios, signal regions with different jet multiplicity requirements and either specific ranges of kinematic variables (multi-bin search) or values of the BDT output variable (BDT search) are defined. An additional set of optimized single-bin signal regions used for a model-independent presentation of the results are also defined. All sets of signal regions used in this document are summarized in the following.

5.1 The multi-bin search

In this search, three sets of signal regions targeting different scenarios with direct decays of squarks and gluinos are defined: the MB-SSd and MB-GGd regions target scenarios with large mass difference between the pair-produced squarks or gluinos and the lightest neutralino, respectively, while the MB-C regions target scenarios with small mass difference between the pair-produced squarks or gluinos and the $\tilde{\chi}_1^0$. Events are assigned to orthogonal bins based on the jet multiplicity, the effective mass and the missing transverse momentum significance defined as $E_T^{\text{miss}}/\sqrt{H_T}$, where H_T is calculated as a scalar sum of transverse momenta of all jets with $p_T > 50$ GeV and $|\eta| < 2.8$. This variable suppresses backgrounds from which jet energy mismeasurement generates missing transverse momentum, and was found to enhance sensitivity to models characterized by the $\tilde{q}\tilde{q}$ production.

After preselecting events as in Table 2, the following selection criteria are applied for the three sets of signal regions, to further suppress the background processes. At least two jets with $|\eta| < 2$ are required for MB-SSd regions, where the p_T of the sub-leading jet must be greater than 100 GeV. The MB-C regions rely on the selection of an energetic ISR jet with $p_T > 600$ GeV. In the MB-GGd regions, at least four jets with $p_T > 100$ GeV, and $|\eta| < 2$ are required. The smallest azimuthal separation between the $\mathbf{p}_T^{\text{miss}}$ and the momenta of up to three leading jets, and remaining jets in the event, $\Delta\phi(j_{1,2,(3)}, \mathbf{p}_T^{\text{miss}})_{\text{min}}$ and $\Delta\phi(j_{i>3}, \mathbf{p}_T^{\text{miss}})_{\text{min}}$, are required to be greater than 0.4 and 0.2, respectively, in all regions except in MB-SSd, where the tighter requirements of 0.8 and 0.4, respectively, are placed. These requirements are designed to reduce the background from multi-jet processes, where a jet can be mismeasured and generate missing

transverse momentum that points along the axis of the jet. In the regions with at least four jets in the final state, jets from signal processes are distributed isotropically. The aplanarity variable, defined as $A = 3/2\lambda_3$ (where λ_3 is the smallest eigenvalue of the normalized momentum tensor of the jets [79]), is therefore used in the MB-GGd regions, with a requirement of $A > 0.04$.

The missing transverse momentum significance is required to be $E_T^{\text{miss}}/\sqrt{H_T} > 10 \text{ GeV}^{1/2}$ and $m_{\text{eff}} > 1000 \text{ GeV}$ in all signal regions except in MB-C, where the tighter, $m_{\text{eff}} > 1600 \text{ GeV}$ requirement is applied. An overview of the signal region preselection criteria applied to the MB-SSd, MB-GGd and MB-C regions is presented in Table 3.

	MB-SSd	MB-GGd	MB-C
N_j	≥ 2	≥ 4	≥ 2
$p_T(j_1) [\text{GeV}]$	> 200	> 200	> 600
$p_T(j_{i=2, \dots, N_{j_{\text{min}}}}) [\text{GeV}]$	> 100	> 100	> 50
$ \eta(j_{i=1, \dots, N_{j_{\text{min}}}}) $	< 2.0	< 2.0	< 2.8
$\Delta\phi(j_{1,2,(3)}, \mathbf{p}_T^{\text{miss}})_{\text{min}}$	> 0.8	> 0.4	> 0.4
$\Delta\phi(j_{i>3}, \mathbf{p}_T^{\text{miss}})_{\text{min}}$	> 0.4	> 0.2	> 0.2
Aplanarity	-	> 0.04	-
$E_T^{\text{miss}}/\sqrt{H_T} [\text{GeV}^{1/2}]$	> 10	> 10	> 10
$m_{\text{eff}} [\text{GeV}]$	> 1000	> 1000	> 1600

Table 3: Summary of preselection criteria used for the multi-bin search.

Following these selections, the SRs are split into multiple bins defined to maximize the sensitivity in the $m(\tilde{q}), m(\tilde{\chi}_1^0)$ or $m(\tilde{g}), m(\tilde{\chi}_1^0)$ planes. The MB-SSd regions are separated into two jet multiplicity bins, up to six bins in m_{eff} and up to four bins in $E_T^{\text{miss}}/\sqrt{H_T}$. In order to reduce the total number of signal regions without significant loss of the search power, some bins are merged as represented schematically in Table 4.

Since the preselection already requires at least four high- p_T jets, the final MB-GGd signal regions are defined by the six bins in m_{eff} and three bins in $E_T^{\text{miss}}/\sqrt{H_T}$, as shown in Table 5.

The final MB-C signal regions are defined by three bins in jet multiplicity, three bins in m_{eff} and two bins in $E_T^{\text{miss}}/\sqrt{H_T}$, as shown in Table 6.

$N_j = [2, 3]$		$m_{\text{eff}} [\text{TeV}]$					
		[1.0, 1.6)	[1.6, 2.2)	[2.2, 2.8)	[2.8, 3.4)	[3.4, 4.0)	[4.0, ∞)
$E_T^{\text{miss}}/\sqrt{H_T} [\text{GeV}^{1/2}]$	[10, 16)						
	[16, 22)						
	[22, 28)						
	[28, ∞)						
$N_j = [4, \infty)$		$m_{\text{eff}} [\text{TeV}]$					
		[1.0, 1.6)	[1.6, 2.2)	[2.2, 2.8)	[2.8, ∞)		
$E_T^{\text{miss}}/\sqrt{H_T} [\text{GeV}^{1/2}]$	[10, 16)						
	[16, 22)						
	[22, ∞)						

Table 4: Summary of the bin boundaries for the MB-SSd signal regions. The highest bin in each case is inclusive.

$N_j = [4, \infty)$		$m_{\text{eff}} [\text{TeV}]$					
		[1.0, 1.6)	[1.6, 2.2)	[2.2, 2.8)	[2.8, 3.4)	[3.4, 4.0)	[4.0, ∞)
$E_T^{\text{miss}}/\sqrt{H_T} [\text{GeV}^{1/2}]$	[10, 16)						
	[16, 22)						
	[22, ∞)						

Table 5: Summary of the bin boundaries for the MB-GGd signal regions. The highest bin in each case is inclusive.

$N_j = [2, 3]; 4; [5, \infty)$		$m_{\text{eff}} [\text{TeV}]$		
		[1.6, 2.2)	[2.2, 2.8)	[2.8, ∞)
$E_T^{\text{miss}}/\sqrt{H_T} [\text{GeV}^{1/2}]$	[16, 22)			
	[22, ∞)			

Table 6: Summary of the bin boundaries for the MB-C signal regions. The highest bin in each case is inclusive.

5.2 The BDT search

This search is performed separately in two sets of signal regions targeting models with gluino-pair production with direct (BDT-GGd) or one-step (BDT-GGo) \tilde{g} decays. In each set, events are separated into four categories, depending on the mass difference $\Delta m(\tilde{g}, \tilde{\chi}_1^0)$ of the target model. The values of $\Delta m(\tilde{g}, \tilde{\chi}_1^0)$ targeted by each of these SRs are indicated in the last rows of Table 7.

After applying the preselection criteria from Table 2, additional selection criteria are applied to the BDT-GGd and BDT-GGo signal regions to further distinguish between signal and background processes. All BDT-GGd regions require the presence of at least four jets, with $\Delta\phi(j_{i>3}, E_T^{\text{miss}})_{\min} \geq 0.4$, and $E_T^{\text{miss}}/m_{\text{eff}}(4j) \geq 0.2$ to further suppress the multi-jet background. Additionally, $E_T^{\text{miss}}/m_{\text{eff}}(Nj) \geq 0.2$ is required in all regions. The BDT-GGo regions require the presence of at least six (BDT-GGo1 and BDT-GGo2) or five (BDT-GGo3 and BDT-GGo4) jets, with $\Delta\phi(j, p_T^{\text{miss}})_{\min} \geq 0.4$ in all regions except in BDT-GGo4, where a looser requirement of $\Delta\phi(j, p_T^{\text{miss}})_{\min} \geq 0.2$ is placed. To select events close to the kinematic regions of interest, $m_{\text{eff}} > 1400$ GeV is required in the BDT-GGd1, BDT-GGd2, BDT-GGo1 and BDT-GGo2 regions, and $m_{\text{eff}} > 800$ GeV in the BDT-GGd3, BDT-GGd4, BDT-GGo3 and BDT-GGo4 regions.

A BDT discriminant is then used to achieve the best sensitivity. In this approach, eight independent BDTs are trained separately for events passing the selection criteria described above. In order to increase the statistics of the signal MC samples used for BDT training, and at the same time keep the output performance stable, signal MC events with similar mass differences between \tilde{g} and $\tilde{\chi}_1^0$ (leading to similar event kinematics), normalized to their corresponding cross-sections, are combined into a single sample for training. All MC samples for the SM background processes listed in Table 1 are taken into account. The multi-jet background events are not used in the BDT training since the contribution of these processes is expected to be negligible. All MC events used in the BDT training are randomly divided into two sets. In order to avoid a decrease of the total MC statistics to a half of the full dataset, the BDT training is performed on both sets of events. The BDT score calculated using one set of events is applied to the other set, which is then used as input for the signal and background evaluation. The data events used for the evaluation are also randomly divided into two sets. Up to 12 variables are selected among E_T^{miss} , m_{eff} , aplanarity, p_T and η of selected jets, and used in the training for the eight signal regions. The selections

based on the BDT scores providing the maximal sensitivity for a benchmark signal model are then used to define the signal regions. The resulting signal region definitions are shown in Table 7.

	BDT-GGd1	BDT-GGd2	BDT-GGd3	BDT-GGd4
N_j	≥ 4			
$\Delta\phi(j_{1,2,(3)}, \mathbf{p}_T^{\text{miss}})_{\text{min}}$	≥ 0.4			
$\Delta\phi(j_{i>3}, \mathbf{p}_T^{\text{miss}})_{\text{min}}$	≥ 0.4			
$E_T^{\text{miss}}/m_{\text{eff}}(Nj)$	≥ 0.2			
$m_{\text{eff}} [\text{GeV}]$	≥ 1400		≥ 800	
BDT score	≥ 0.97	≥ 0.94	≥ 0.94	≥ 0.87
$\Delta m(\tilde{g}, \tilde{\chi}_1^0) [\text{GeV}]$	1600 – 1900	1000 – 1400	600 – 1000	200 – 600

	BDT-GGo1	BDT-GGo2	BDT-GGo3	BDT-GGo4
N_j	≥ 6			
$\Delta\phi(j_{1,2,(3)}, \mathbf{p}_T^{\text{miss}})_{\text{min}}$	≥ 0.4			
$\Delta\phi(j_{i>3}, \mathbf{p}_T^{\text{miss}})_{\text{min}}$	≥ 0.4			
$E_T^{\text{miss}}/m_{\text{eff}}(Nj)$	≥ 0.2			
$m_{\text{eff}} [\text{GeV}]$	≥ 1400		≥ 800	
BDT score	≥ 0.96	≥ 0.87	≥ 0.92	≥ 0.84
$\Delta m(\tilde{g}, \tilde{\chi}_1^0) [\text{GeV}]$	1400 – 2000	1200 – 1400	600 – 1000	200 – 400

Table 7: Signal region selections for the BDT search with the benchmark signal model parameters ($\Delta m(\tilde{g}, \tilde{\chi}_1^0)$) used in the optimisation, for (top) direct and (bottom) one-step gluino decays, respectively.

5.3 Model independent selections

In addition to the multi-bin and BDT searches described above, several signal regions, optimized to maximize the sensitivity to SUSY models resulting with various jet multiplicities in the final state, are defined. These signal regions rely on the single-bin approach as in Ref. [13], and are designed in order to compute the statistical significance in a model-independent way. After applying the preselection criteria of Table 2, ten inclusive SRs characterized by increasing minimum jet multiplicity are defined as in Tables 8 and 9. Some of them require the same jet-multiplicity, but are distinguished by requiring higher m_{eff} values. These regions overlap, and therefore cannot be combined statistically.

	SR2j-1600	SR2j-2200	SR2j-2800	SR4j-1000	SR4j-2200	SR4j-3400
N_j	≥ 2				≥ 4	
$p_T(j_1) [\text{GeV}]$	> 250	> 600	> 250		> 200	
$p_T(j_{i=2, \dots, N_{j_{\text{min}}}}) [\text{GeV}]$	> 250	> 50	> 250		> 100	
$ \eta(j_{i=1, \dots, N_{j_{\text{min}}}}) $	< 2.0	< 2.8	< 1.2		< 2.0	
$\Delta\phi(j_{1,2,(3)}, \mathbf{p}_T^{\text{miss}})_{\text{min}}$	> 0.8	> 0.4	> 0.8		> 0.4	
$\Delta\phi(j_{i>3}, \mathbf{p}_T^{\text{miss}})_{\text{min}}$	> 0.4	> 0.2	> 0.4		> 0.4	
Aplanarity	–			> 0.04		
$E_T^{\text{miss}}/\sqrt{H_T} [\sqrt{\text{GeV}}]$	> 16				> 10	
$m_{\text{eff}} [\text{GeV}]$	> 1600	> 2200	> 2800	> 1000	> 2200	> 3400

Table 8: Selection criteria used for model-independent search regions with jet multiplicities up to four.

	SR5j-1600	SR6j-1000	SR6j-2200	SR6j-3400
N_j	≥ 5		≥ 6	
$p_T(j_1)$ [GeV]	> 600		> 200	
$p_T(j_{i=2, \dots, N_{j_{\min}}})$ [GeV]	> 50		> 75	
$ \eta(j_i = 1, \dots, N_{j_{\min}}) $	< 2.8		< 2.0	
$\Delta\phi(j_{1,2,(3)}, p_T^{\text{miss}})_{\min}$			> 0.4	
$\Delta\phi(j_{i>3}, p_T^{\text{miss}})_{\min}$			> 0.2	
Aplanarity	-		> 0.08	
$E_T^{\text{miss}}/\sqrt{H_T}$ [GeV]		> 16		> 10
m_{eff} [GeV]	> 1600	> 1000	> 2200	> 3400

Table 9: Selection criteria used for model-independent search regions with high jet multiplicities.

6 Background estimation

Standard Model background processes contribute to the event counts in the signal regions. The backgrounds in both searches are: Z -jets, W -jets, top quark pair, single top quark, diboson and multi-jet production. Non-collision backgrounds have been found to be negligible.

Generally, the Z -jets background events originate from an irreducible component in which $Z \rightarrow v\bar{v}$ decays generate large E_T^{miss} . The W -jets background is mostly composed of $W \rightarrow \tau\nu$ events in which the τ -lepton decays to hadrons, with additional contributions from $W \rightarrow e\nu, \mu\nu$ events in which no baseline electron or muon is reconstructed, with E_T^{miss} due to neutrinos. Top quark pair production, followed by semileptonic decays, in particular $t\bar{t} \rightarrow b\bar{b}\tau\nu qq'$ (with the τ -lepton decaying to hadrons), as well as single-top-quark events, can also generate large E_T^{miss} and satisfy the jet and lepton-veto requirements. Each of these primary backgrounds is estimated using dedicated control regions, as described in the following section, while diboson production is estimated with MC simulated data normalized using NLO cross-section predictions, as described in Section 3.

The multi-jet background in the signal regions is due to missing transverse momentum from misreconstruction of jet energies in the calorimeters, jets lost due to the JVT requirement, as well as neutrinos from semileptonic decays of heavy-flavor hadrons. It is estimated in a data-driven way described below.

6.1 Control regions

To estimate the SM backgrounds in an accurate and robust fashion, control regions (CRs) are defined for each of the signal regions. They are chosen to be orthogonal to the SR selections in order to provide independent data samples enriched in particular backgrounds and are used to normalize the background MC simulation. The CR selections are optimized to have negligible expected SUSY signal contamination for the models near the previous exclusion boundary. Cross-checks of the background estimates are performed with data in several validation regions (VRs) selected with requirements such that these regions do not overlap with the CR and SR selections and also have a low expected signal contamination.

Four control regions are defined for each signal region used in the searches documented here. The CR selections are optimized to maintain adequate statistical precision while minimizing the systematic uncertainties arising from the extrapolation of the CR event yield to estimate the background in the SR. This latter requirement is addressed through the use of CR jet p_T thresholds and m_{eff} selections which

match those used in the SR. In some cases, in order to increase the number of CR data events without significantly increasing the theoretical uncertainties associated with the background estimation procedure, some SR selection requirements are omitted or loosened, as indicated in the text below. The CR definitions are listed in Table 10.

CR	SR background	CR process	CR selection
MB/BDT-CR γ	$Z(\rightarrow \nu\bar{\nu})$ +jets	γ +jets	Isolated photon
MB/BDT-CRQ	Multi-jet	Multi-jet	reversed requirements on (i) $\Delta\phi(j, \mathbf{p}_T^{\text{miss}})$ and (ii) $E_T^{\text{miss}}/m_{\text{eff}}(N_j)$ or $E_T^{\text{miss}}/\sqrt{H_T}$
MB/BDT-CRW	$W(\rightarrow \ell\nu)$ +jets	$W(\rightarrow \ell\nu)$ +jets	one lepton, $30 \text{ GeV} < m_T(\ell, E_T^{\text{miss}}) < 100 \text{ GeV}$, b -veto
MB/BDT-CRT	$t\bar{t}$ (+EW) and single top	$t\bar{t} \rightarrow b\bar{b}qq'\ell\nu$	one lepton, $30 \text{ GeV} < m_T(\ell, E_T^{\text{miss}}) < 100 \text{ GeV}$, b -tag

Table 10: Control regions used in the analysis. Also listed are the main targeted background in the SR in each case, the process used to model the background, and the main CR requirement(s) used to select this process. The jet p_T thresholds and m_{eff} selections match those used in the corresponding SRs.

The γ +jets region in both searches (labeled as MB/BDT-CR γ Table 10) is used to estimate the contribution of $Z(\rightarrow \nu\bar{\nu})$ +jets background events to each SR by selecting a sample of γ +jets events with $p_T(\gamma) > 150 \text{ GeV}$ and then treating the reconstructed photon as contributing to E_T^{miss} . For $p_T(\gamma)$ significantly larger than m_Z the kinematic properties of such events strongly resemble those of Z +jets events [80]. In order to correct the difference in the Z +jets and γ +jets ratio between data and MC, a correction factor is applied to simulated γ +jets events in CR γ regions. This correction factor, calculated separately for regions with up to three and at least four jets, $\kappa = 0.77 \pm 0.04$ and $\kappa = 0.85 \pm 0.05$ respectively, is determined by comparing CR γ observations with those in the regions defined by selecting events with two electrons or muons for which the invariant mass lies within 25 GeV of the mass of the Z boson, satisfying $E_T^{\text{miss}}/\sqrt{H_T} > 10 \text{ GeV}^{1/2}$ and $m_{\text{eff}} > 1000 \text{ GeV}$. This selection corresponds to the kinematically lowest bins of the multi-bin analysis MB-SSd with $N_j=[2, 3]$ and $N_j=[4, \infty]$. The uncertainty presented for these correction factors is statistical only. In both searches described in this document, CR γ selections omit the SR requirement on the aplanarity variable. Additionally, for BDT-GGo1 and BDT-GGo2 SRs, the $\Delta\phi(j, \mathbf{p}_T^{\text{miss}})$, and $E_T^{\text{miss}}/m_{\text{eff}}(N_j)$ selections are removed for the corresponding CR selections.

The W and top regions in both searches (labeled as MB/BDT-CRW and MB/BDT-CRT in Table 10) aim to select samples rich in $W(\rightarrow \ell\nu)$ +jets and semileptonic $t\bar{t}$ and single top background events, respectively. They use events with one high-purity lepton and differ in their number of b -jets (zero or ≥ 1 , respectively). In both searches, the requirement on the transverse mass m_T computed with the E_T^{miss} and the selected lepton² is applied, as indicated in Table 10. In order to increase statistics in these regions, events are selected using a trigger based on the missing transverse momentum as described in Section 2. This approach allows using leptons with transverse momenta down to 6 GeV for muons and 7 GeV for electrons, which brings the CRs closer to the SR phase-space. The selected lepton is treated as a jet with the same momentum to model background events in which a hadronically decaying τ -lepton is produced. The CRW and CRT selections omit the SR selection requirements on $\Delta\phi(j, \mathbf{p}_T^{\text{miss}})$, in both searches. For the multi-bin search, only the requirement on the $E_T^{\text{miss}}/\sqrt{H_T}$ as indicated in Table 3 is used, in order to increase the number of CR data events without significantly increasing the theoretical uncertainties associated with the background estimation procedure. Multi-bin regions selected with the same m_{eff} and N_j bin but different $E_T^{\text{miss}}/\sqrt{H_T}$ bin share the same control region.

² $m_T = \sqrt{2p_T^\ell E_T^{\text{miss}}(1 - \cos[\Delta\phi(\ell, \mathbf{p}_T^{\text{miss}})])}$.

The multi-jet background in both searches is estimated using a data-driven technique [80], which applies a jet resolution function to well-measured multi-jet events in order to estimate the impact of jet energy mismeasurement and heavy-flavor semileptonic decays on E_T^{miss} and other variables. The resolution function of jets is initially estimated from MC simulation by matching jets reconstructed from generator-level particles including muons and neutrinos to detector-level jets in multi-jet samples, and then is modified to agree with data in dedicated samples used to measure the resolution function. The multi-jet region (labeled as MB/BDT-CRQ in Table 10) uses reversed selection requirements on $\Delta\phi(j, p_T^{\text{miss}})$ and on $E_T^{\text{miss}}/\sqrt{H_T}$ in the multi-bin search, or on $E_T^{\text{miss}}/m_{\text{eff}}(N_j)$ in the case of the BDT search, to produce samples enriched in multi-jet background events. For the two signal regions targeting lowest mass splittings in the BDT search, BDT-GGd4 and BDT-GGo4, the BDT score selections are slightly loosened from 0.87 to 0.70 and from 0.84 to 0.60, respectively. The MB/BDT-CRQ regions are used to normalize the shape of the distributions obtained with the data-driven technique.

In order to estimate the background yields, a background-only fit is used [81]. The fit is performed using the observed event yields in the CRs associated with the SRs as the only constraints, but not the yields in the SRs themselves. It is assumed that signal events from beyond the Standard Model (BSM) processes do not contribute to these CR yields. The scale factors represent the normalization of background components relative to MC predictions ($\mu(W+\text{jets})$, $\mu(Z+\text{jets})$, $\mu(\text{Top})$), and are simultaneously determined in the fit to all the CRs associated with a SR. The expected background in the SR is based on the yields predicted by simulation for $W/Z+\text{jets}$ and background processes containing top quarks, corrected by the scale factors derived from the fit. The systematic and MC statistical uncertainties on the expected values are included in the fit as nuisance parameters that are constrained by Gaussian distributions with widths corresponding to the sizes of the uncertainties considered and by Poisson distributions, respectively. The background-only fit is also used to estimate the background event yields in the validation regions (VR). The normalization factors determined from the background-only fits in each CR for each background process are shown in Figure 2. Some trends in these factors are observed, with the normalization factors for top background becoming smaller with increasingly tight selection requirements for the multi-bin search signal regions. Similarly, the measured top normalization factors decrease with increasingly tight BDT score requirements in the BDT search. This behavior follows from the simulated top MC samples exhibiting generally harder kinematics than observed in data [82]. Before the top normalization factors are applied, the contribution of the top background was expected to be less than 10% (typically 1-2%) in most of the signal regions, with the exception of signal regions with very tight kinematic selections where the contribution of the top background reaches up to 50% of the total background yield. The normalization factors for $W+\text{jets}$ and $Z+\text{jets}$ processes are generally stable with changing kinematic selections.

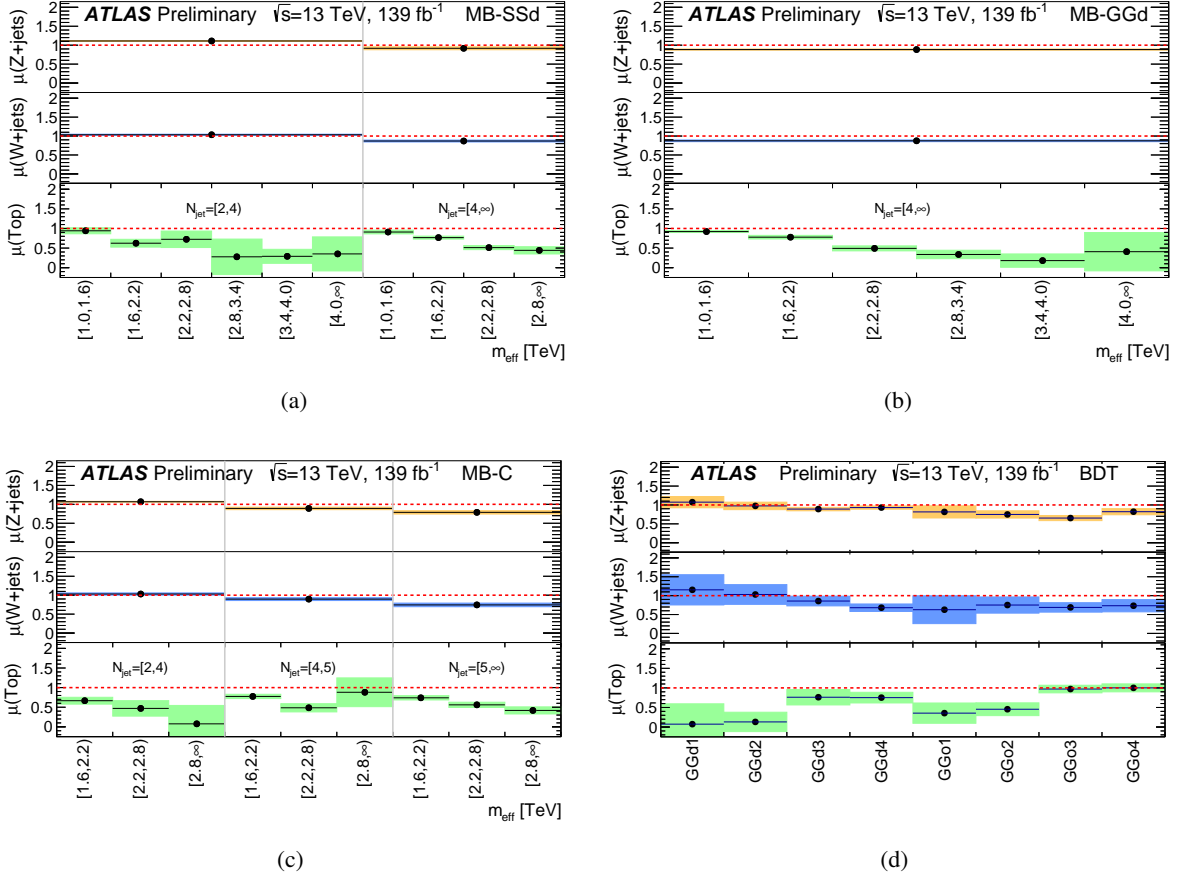


Figure 2: Fitted normalization factors per process as a function of the signal region considered in the (a) MB-SSd, (b) MB-GGd, (c) MB-C regions from the multi-bin, and (d) regions from the BDT search. The dashed horizontal lines at 1 correspond to pure MC estimates with the vertical size of the colored regions corresponding to the total uncertainty in each background source.

Example m_{eff} distributions in control regions based on MB-GGd preselection requirements listed in Table 3 are shown in Figure 3. Figure 4 shows the BDT score discriminating variable distributions in control regions corresponding to the BDT-GGo1 signal region selections.

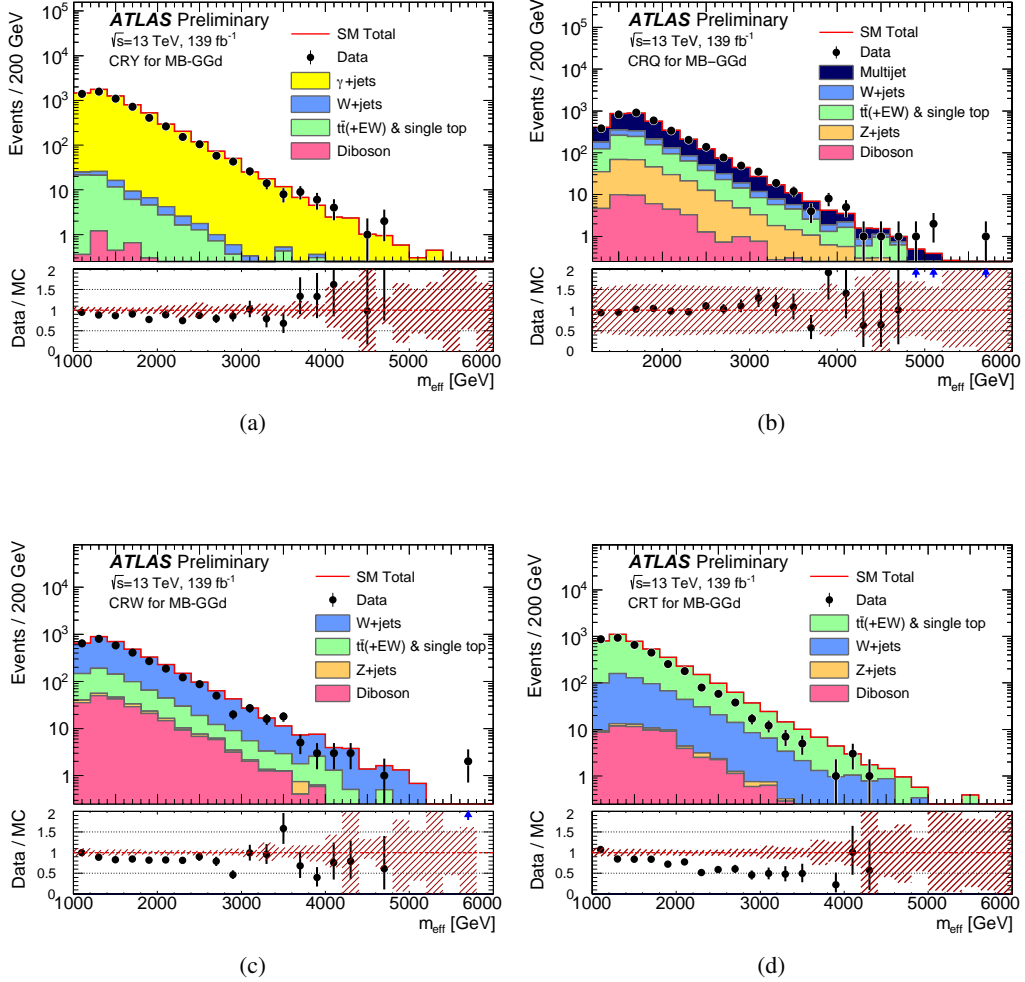


Figure 3: Observed m_{eff} distributions in control regions (a) MB-CR γ , (b) MB-CRQ, (c) MB-CRW and (d) MB-CRT after applying the MB-GGd preselection requirements listed in Table 3. The histograms show the MC background predictions normalized using cross-section times integrated luminosity, with the exception of multi-jet background which is normalized using data. In the case of the γ +jets background, a κ factor described in the text is applied. The last bin includes overflow events. The hatched (red) error bands indicate the combined experimental and MC statistical uncertainties.

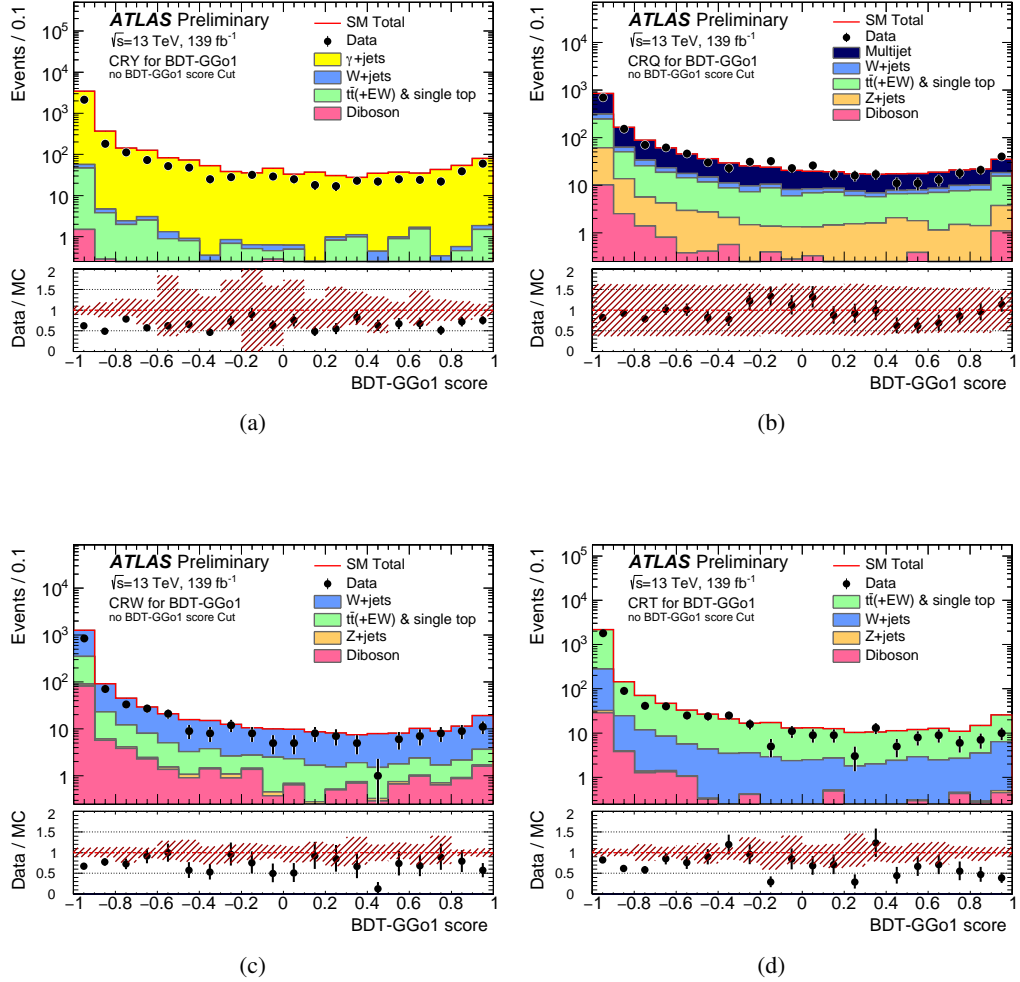


Figure 4: Observed BDT score distributions in control regions (a) BDT-CR γ , (b) BDT-CRQ, (c) BDT-CRW and (d) BDT-CRT after applying the BDT-GGo1 selection requirements described in Section 5.2. The histograms show the MC background predictions normalized using cross-section times integrated luminosity, with the exception of multi-jet background which is normalized using data. In the case of the γ +jets background, a κ factor described in the text is applied. The hatched (red) error bands indicate the combined experimental and MC statistical uncertainties.

6.2 Validation regions

The background estimation procedure is validated by comparing the numbers of events observed in the VRs to the corresponding SM background predictions obtained from the background-only fits. Several VRs are defined in both searches, with requirements distinct from those used in the CRs and that maintain low expected signal contamination. Like the CRs, the majority of the VRs are defined in final states with leptons and photons, allowing the different expected background contributions to the SRs to be validated independently with high-purity selections.

The MB/BDT-CR γ estimates of the $Z(\rightarrow \nu\bar{\nu})$ +jets background are validated using samples of $Z(\rightarrow \ell\bar{\ell})$ +jets events selected by requiring high-purity lepton pairs of opposite sign and identical flavor for which the dilepton invariant mass lies within 25 GeV of the Z boson mass (MB/BDT-VRZ). Events are selected by the trigger requiring at least one isolated electron or muon, as described in Section 2. In the MB/BDT-VRZ regions, the leptons are treated as contributing to E_T^{miss} . In order to increase statistics in these selections due to the smaller branching ratio for $Z \rightarrow \ell\ell$ ($\ell = e, \mu$) compared to $Z \rightarrow \nu\nu$, a looser selection with respect to that used for the SR is necessary. For this reason MB/BDT-VRZ is defined to follow the SR selection with no requirements based on $\Delta\phi(j, \mathbf{p}_T^{\text{miss}})$, $E_T^{\text{miss}}/m_{\text{eff}}(N_j)$ (or $E_T^{\text{miss}}/\sqrt{H_T}$) and aplanarity. To validate the extrapolation over these variables from dedicated CRs to the SRs, additional validation regions, BDT-VRZf, MB/BDT-VRZdPhi, MB-VRZMETsig and BDT-VRZAp are defined by applying the full set of corresponding SR selection requirements, or by adding selection based on $\Delta\phi(j, \mathbf{p}_T^{\text{miss}})$, $E_T^{\text{miss}}/m_{\text{eff}}(N_j)$ (or $E_T^{\text{miss}}/\sqrt{H_T}$) and aplanarity, respectively, to the corresponding VRZ selection. By definition, events selected by the BDT-VRZf region overlap with a subset of events selected by the BDT-VRZdPhi and BDT-VRZAp regions.

The MB/BDT-CRW and MB/BDT-CRT estimates of the W +jets and top background are validated starting with the same MB/BDT-CRW and MB/BDT-CRT selections. In order to validate the extrapolation over the $\Delta\phi(j, \mathbf{p}_T^{\text{miss}})$, $E_T^{\text{miss}}/m_{\text{eff}}(N_j)$ or $E_T^{\text{miss}}/\sqrt{H_T}$, and aplanarity variables from the dedicated W +jets and top CRs to the SRs, validation regions MB/BDT-VRWdPhi, MB-VRWMETsig and BDT-VRWAp, as well as MB/BDT-VRTdPhi, MB-VRTMETsig and BDT-VRTAp are defined respectively, by applying a selection requirement on the corresponding variable as in the SR selection. In addition, validation regions BDT-VRWf and BDT-VRTf are defined to follow the full event selection criteria as in the corresponding SR, not including the lepton veto.

The MB/BDT-CRQ estimates of the multi-jet background are validated with VRs for which the MB/BDT-CRQ selection is applied, but with the SR $E_T^{\text{miss}}/\sqrt{H_T}$ (MB-VR0LMETsig), $E_T^{\text{miss}}/m_{\text{eff}}(N_j)$ (BDT-VR0LMETEff) requirements reinstated, or with a requirement on $\Delta\phi(j, \mathbf{p}_T^{\text{miss}})$ applied (MB/BDT-VR0LdPhi). These VRs called VR0L are dedicated not only to test the multi-jet background, but all backgrounds in 0-lepton channel.

For the BDT search, the BDT score is loosened until a minimum of 10 predicted background events is obtained. These regions used to validate BDT-CR γ , BDT-CRW and BDT-CRT are labelled as BDT-VRZL, BDT-VRWL and BDT-VRTL, respectively.

The results of the validation procedure are shown in Figures 5 and 6, where the compatibility of the observed and expected event yields in validation regions, VR0Ls, designed to test all backgrounds in the 0-lepton channel, are summarized. No significant systematic biases are observed among all the 448 VR used in both searches. The largest discrepancy is 2.6σ in the MB-VR0LMETsig region associated with the MB-SSd signal region that selects events with two or three jets in the m_{eff} bin [2800, 3400) GeV, with $E_T^{\text{miss}}/\sqrt{H_T}$ bin requirement [16, 22) GeV $^{1/2}$ reinstated. In the BDT search, the largest discrepancy of 2.4σ is found in the BDT-VRTL region associated with the BDT-GGo2 signal region. The quoted significance is computed following the profile likelihood method of Ref. [83] including the systematics uncertainties described in Section 7.

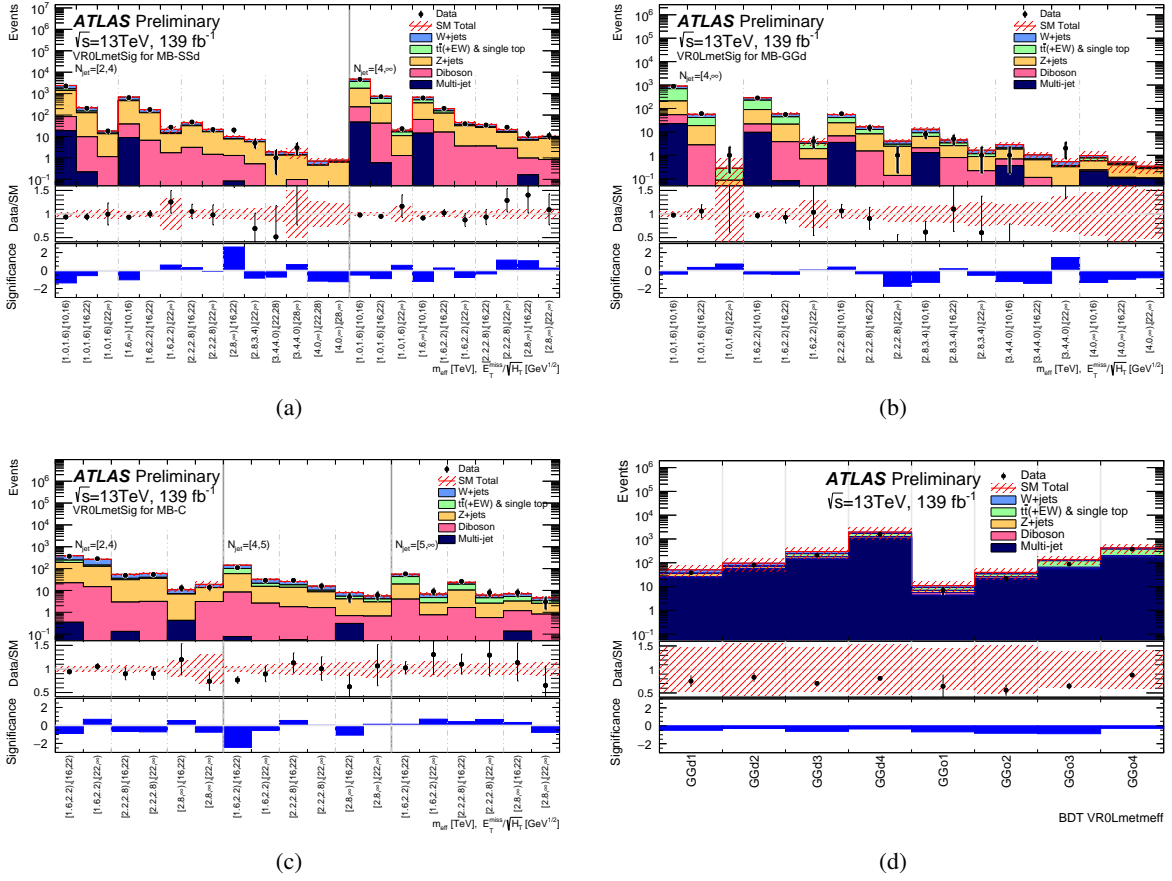


Figure 5: Differences between the numbers of observed events in data and the SM background predictions for VR0LMETSig used in the (a) MB-SSd, (b) MB-GGd, (c) MB-C regions from the multi-bin, and (d) BDT-VR0LMETMeff regions from the BDT search. The significance is computed following the profile likelihood method of Ref. [83] in the case where the observed yield exceeds the prediction, and using the same expression with an overall minus sign if the yield is below the prediction.

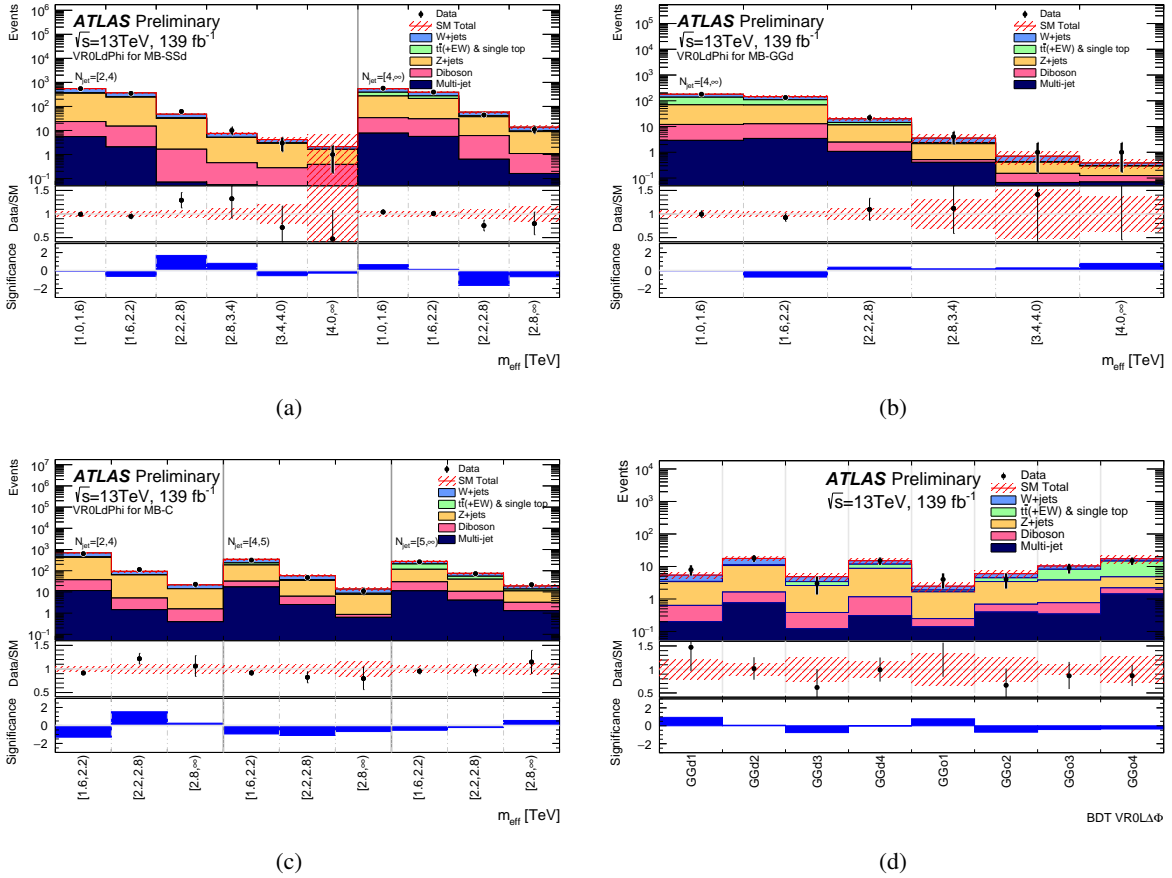


Figure 6: Differences between the numbers of observed events in data and the SM background predictions for MB-VR0LdPhi used in the (a) MB-SSd, (b) MB-GGd, (c) MB-C regions from the multi-bin, and (d) BDT-VR0LdPhi regions from the BDT search. The significance is computed following the profile likelihood method of Ref. [83] in the case where the observed yield exceeds the prediction, and using the same expression with an overall minus sign if the yield is below the prediction.

7 Systematic uncertainties

The systematic uncertainties (experimental and theoretical) on the background estimates are evaluated for the extrapolation factors that relate observations in the control regions to background predictions in the signal regions and on the MC modeling of minor backgrounds. They are incorporated in the likelihood fit as nuisance parameters, which are constrained by Gaussian terms. The mean of the Gaussian is defined by the nominal prediction, while the standard deviation is determined by the size of the systematic uncertainty. Poisson distributions are used for the statistical uncertainties arising from the limited number of data events in the estimation of the background sources, or the limited number of simulated events.

The overall background uncertainties, detailed in Figure 7, range from 5% in most of the MB-SSd regions to 60% in MB-GGd region which imposes tight requirements on m_{eff} and $E_{\text{T}}^{\text{miss}}/\sqrt{H_{\text{T}}}$, and from 8% in BDT-GGd3 to 28% in BDT-GG01 region.

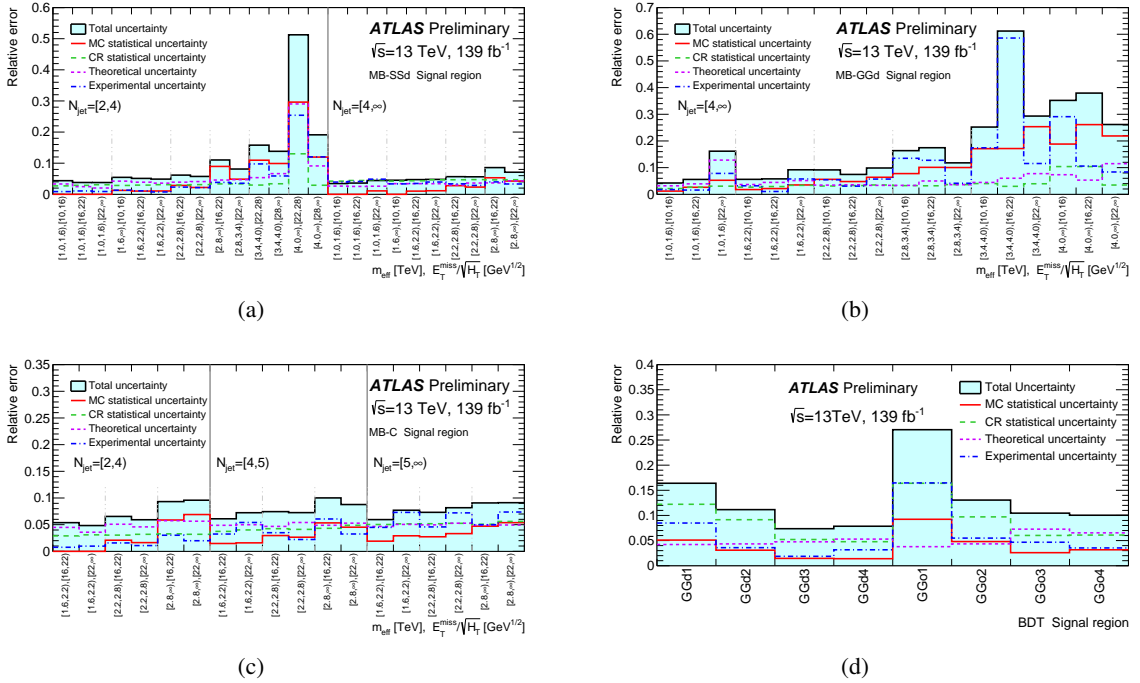


Figure 7: Breakdown of the largest systematic uncertainties in the background estimates for the (a) MB-SSd, (b) MB-GGd, (c) MB-C regions from the multi-bin, and (d) regions from the BDT search. The individual uncertainties can be correlated, such that the total background uncertainty is not necessarily their sum in quadrature.

For the backgrounds estimated with MC simulation-derived extrapolation factors, the primary common sources of systematic uncertainty are the jet energy scale (JES) calibration, jet energy resolution (JER), theoretical uncertainties in the modelling of these backgrounds, and limited event yields in the MC samples and data CRs. Correlations between uncertainties (for instance between JES or JER uncertainties in CRs and SRs) are taken into account where appropriate.

The JES and JER uncertainties are estimated using the methods discussed in Refs. [84, 85]. Variations according to the scale and resolution of the missing transverse momentum are also considered [77]. The combined JES, JER and E_T^{miss} uncertainty ranges from 1% of the expected background in multi-bin signal regions which select events with two jets, to $\sim 60\%$ in MB-GGd region with tight requirements on m_{eff} and $E_T^{\text{miss}}/\sqrt{H_T}$. In the BDT search, the same uncertainties range from 1% in BDT-GGd3 to 15% in BDT-GG01 region.

Uncertainties arising from theoretical modeling of background processes are estimated by comparing samples produced with different MC generators or by varying the renormalization and factorization scales.

The $W/Z+\text{jets}$ modelling uncertainties are estimated by considering different merging (CKKW-L) and resummation scales using alternative samples, PDF and strong coupling constant (α_s) variations from the NNPDF3.0NNLO replicas, and variations of factorisation and renormalisation scales in the matrix element. The latter have been evaluated using 7 point-variations, changing the renormalisation and factorisation scales up and down by factors 0.5 and 2, such that when one scale is up the other is down, and vice-versa. Uncertainties in the modeling of top quark pair production are estimated by comparing the nominal sample

listed in Table 1 with the alternative samples. The systematic uncertainty due to the hard-scattering process is evaluated using a comparison of the nominal sample with the sample generated with MG5_aMC@NLO interfaced to PYTHIA 8. Fragmentation and hadronisation uncertainties are assessed using a comparison of the nominal sample with a sample generated with POWHEG-Box interfaced to the HERWIG 7 [86] package for parton showering. Initial- and final-state radiation uncertainties, as well as the variation of factorisation and renormalisation scales, and variable shower radiation uncertainty, are encapsulated in the dedicated event weights in the nominal sample. Uncertainties in diboson production due to PDF, α_s , renormalization and factorization scale uncertainties are estimated in similar way as for the $W/Z+jets$ modelling uncertainties. The combined theoretical uncertainty ranges from 3% in the multi-bin signal regions with loosest kinematic requirements to 30% in multi-bin signal regions based on very tight kinematic selection, and from 3% to 8% in the BDT search.

The impact of lepton reconstruction uncertainties, and of the uncertainties related to the b -tag/ b -veto efficiency, on the overall background uncertainty is found to be negligible for all SRs.

The uncertainties arising from the data-driven correction procedure applied to events selected in the $CR\gamma$ region, described in Section 6, are included in Figure 7 under ‘CR statistical uncertainty’. The total uncertainties due to CR data sample sizes range from 3% to 14% for multi-bin SRs and from 5% to 16% for BDT SRs. The statistical uncertainty arising from the use of MC samples is largest in MB-SSd and MB-GGd SRs (up to 30%) and BDT-GGo1 SR (8%). A conservative uncertainty related to the multi-jet background estimates is taken into account by applying a uniform 100% uncertainty to the multi-jet yield in all SRs. In most of the SRs these uncertainties are negligible, and the maximum resulting contribution to the overall background uncertainty is less than 1%.

Experimental uncertainties (JES, JER and E_T^{miss}) and MC statistical uncertainty in the SUSY signals are estimated in the same way as for the background and are less than a few percent for most of the signals. The signal cross-section uncertainty is estimated by computing the changes when the renormalization and factorization scale, PDF and the strong coupling constant are varied. The uncertainties in the amount of ISR and FSR in the SUSY signals are estimated by varying generator tunes in the simulation as well as scales used in the matrix-element generator as a function of the mass difference, Δm , between gluino (or squark) and $\tilde{\chi}_1^0$. This uncertainty reaches $\sim 10\%$ in the regions with $\Delta m = 25$ GeV and is negligible for $\Delta m > 200$ GeV.

8 Results, interpretation and limits

Distributions of m_{eff} and $E_T^{\text{miss}}/\sqrt{H_T}$ from the multi-bin search, obtained after applying selection criteria from Table 3, before the final binning selections on this quantity, are shown in Figures 8 and 9 for data and the different MC samples normalized using the theoretical cross-sections. Similarly, distributions of the final discriminating variable used in the BDT search after applying selection criteria from Table 7 are shown in Figure 10, for selected signal regions. Examples of SUSY signals are also shown for illustration. These signals correspond to the processes to which each SR is primarily sensitive: $\tilde{q}\tilde{q}$ production for the lower jet-multiplicity SRs and $\tilde{g}\tilde{g}$ production for the higher jet-multiplicity SRs. In these figures, data and background distributions largely agree within uncertainties.

The number of events observed in the data and the number of SM events expected to enter each of the signal regions determined using the background-only fit are shown in Table 11 for the BDT search and in Table 12 for the model-independent search. The results of all searches presented in this document are also

summarized in Figure 11. To quantify the level of agreement between background predictions and observed yields and to set upper limits on the number of BSM signal events in each SR, a model-independent fit is used [81]. This fit proceeds in the same way as the background-only fit, where yields in the CRs are used to constrain the predictions of backgrounds in each SR, while the SR yield is also used in the likelihood with an additional nuisance parameter describing potential signal contributions. The observed and expected upper limits at 95% confidence level (CL) on the number of events from BSM phenomena for each signal region (S_{obs}^{95} and S_{exp}^{95}) are derived using the CL_s prescription [87], neglecting any possible signal contamination in the CRs. These limits, when normalized by the integrated luminosity of the data sample, may be interpreted as upper limits on the visible cross-section of BSM physics ($\langle \epsilon \sigma \rangle_{\text{obs}}^{95}$), where the visible cross-section is defined as the product of production cross-section, acceptance and efficiency. The model-independent fit is also used to compute the one-sided p -value (p_0) of the background-only hypothesis, which quantifies the statistical significance of an excess. No statistically significant deviation from the background expectation is found for all of the presented searches.

The model-dependent fits [81] in all the SRs are used to set limits on specific classes of SUSY models using asymptotic formulae [88]. Such a fit proceeds in the same way as the model-independent fit, except that both the signal yield in the signal region and the signal contamination in the CRs are taken into account. Correlations between signal and background systematic uncertainties are taken into account where appropriate. Signal-yield systematic uncertainties due to detector effects and the theoretical uncertainties in the signal acceptance are included in the fit. The two searches, multi-bin and BDT search, presented in this paper are combined such that the final observed and expected 95% CL exclusion limits are obtained from the signal regions with the best expected CL_s value.

Figure 12 shows the exclusion limits in simplified models with squark-pair production and subsequent direct squark decays to a quark and the lightest neutralino. For both observed and expected combined limits, the signal region with the best expected sensitivity is used at each point. From the observed limits, neutralino masses below about 850 GeV can be excluded for squark masses of 1300 GeV, and for a massless neutralino squark masses are excluded below 1940 GeV, using the optimized signal regions from the multi-bin search.

Another example of a direct decay is shown in Figure 13, where gluino-pair production with the subsequent decay $\tilde{g} \rightarrow q\tilde{q}\tilde{\chi}_1^0$ is considered. Due to the higher production cross-sections compared to the squark-pair production, higher mass limits can be obtained. For gluino masses up to about 1000 GeV, neutralino masses can be excluded below about 950 GeV or close to the kinematic limit near the diagonal, as obtained by the multi-bin signal regions dedicated to models with compressed mass spectra. For small neutralino masses the observed limit on the gluino mass is as large as 2350 GeV. For gluino masses up to about 1700 GeV the best sensitivity is obtained with the optimized BDT regions, excluding the neutralino masses below about 1160 GeV.

Figure 14 shows the exclusion limits for squark-pair production where the squark decays via an intermediate chargino (one step) to a quark, W boson and neutralino. For the model presented in Figure 14(a) the chargino mass is fixed at $m(\tilde{\chi}_1^\pm) = (m(\tilde{q}) + m(\tilde{\chi}_1^0))/2$ and the result is shown in the $(m(\tilde{q}), m(\tilde{\chi}_1^0))$ plane. In the region close to the kinematic limit near the diagonal, neutralino and squark masses up to 700 GeV are excluded, as obtained by the multi-bin signal regions dedicated to models with compressed mass spectra. For massless neutralino, squark masses are excluded below 1590 GeV. Figure 14(b) shows the exclusion limits in the $(m(\tilde{q}), x)$ plane, where x is defined as $x = \Delta m(\tilde{\chi}_1^\pm, \tilde{\chi}_1^0)/\Delta m(\tilde{q}, \tilde{\chi}_1^0)$, in models in which the neutralino mass is fixed at 60 GeV. Squark masses are excluded up to 1570 GeV for the most favourable x values.

Signal Region	BDT regions			
	GGd1	GGd2	GGd3	GGd4
Fitted background events				
Diboson	3.0 ± 0.9	4.9 ± 1.4	21 ± 5	26 ± 7
$Z/\gamma^* + \text{jets}$	20 ± 4	33 ± 5	139 ± 14	180 ± 18
$W + \text{jets}$	7.0 ± 2.6	13.2 ± 3.5	48 ± 8	52 ± 9
$t\bar{t}(\text{+EW}) + \text{single top}$	$0.1^{+0.3}_{-0.1}$	$0.6^{+0.8}_{-0.6}$	16 ± 5	39 ± 11
Multi-jet	$0.1^{+0.1}_{-0.1}$	$0.1^{+0.1}_{-0.1}$	$0.1^{+0.1}_{-0.1}$	$0.1^{+0.1}_{-0.1}$
Total bkg (pre-fit)	29	56	253	348
Total bkg	30 ± 5	52 ± 6	223 ± 17	298 ± 23
Observed	34	68	227	291
$\langle\epsilon\sigma\rangle_{\text{obs}}^{95} [\text{fb}]$	0.13	0.25	0.33	0.36
S_{obs}^{95}	19	34	46	50
S_{exp}^{95}	16^{+6}_{-5}	22^{+8}_{-5}	43^{+17}_{-12}	54^{+20}_{-15}
$p_0 (Z)$	0.30 (0.52)	0.05 (1.60)	0.44 (0.15)	0.50 (0.00)
Signal Region	GGo1	GGo2	GGo3	GGo4
	Fitted background events			
Diboson	0.6 ± 0.2	2.2 ± 0.6	6.6 ± 2.2	6.8 ± 2.1
$Z/\gamma^* + \text{jets}$	3.8 ± 1.3	10.9 ± 1.9	35 ± 6	39 ± 7
$W + \text{jets}$	0.9 ± 0.5	3.8 ± 1.3	16 ± 4	27 ± 6
$t\bar{t}(\text{+EW}) + \text{single top}$	0.2 ± 0.2	1.3 ± 0.8	28 ± 6	85 ± 14
Multi-jet	—	—	$0.1^{+0.1}_{-0.1}$	$0.5^{+0.5}_{-0.5}$
Total bkg (pre-fit)	7	25	111	178
Total bkg	5.5 ± 1.5	18.3 ± 2.4	85 ± 9	159 ± 16
Observed	6	25	80	135
$\langle\epsilon\sigma\rangle_{\text{obs}}^{95} [\text{fb}]$	0.05	0.12	0.16	0.18
S_{obs}^{95}	7	17	22	25
S_{exp}^{95}	$6.6^{+2.5}_{-1.8}$	11^{+5}_{-2}	25^{+10}_{-7}	37^{+14}_{-10}
$p_0 (Z)$	0.41 (0.22)	0.10 (1.28)	0.50 (0.00)	0.50 (0.00)

Table 11: Numbers of events observed in the signal regions used in the BDT search compared with background expectations obtained from the fits described in the text and from the MC expectations. Empty cells (indicated by a ‘—’) correspond to estimates lower than 0.01. The p-values (p_0) give the probabilities of the observations being consistent with the estimated backgrounds. For an observed number of events lower than expected, the p-value is truncated at 0.5. Between parentheses, p -values are also given as the number of equivalent Gaussian standard deviations (Z). Also shown are 95% CL upper limits on the visible cross-section ($\langle\epsilon\sigma\rangle_{\text{obs}}^{95}$), the visible number of signal events (S_{obs}^{95}) and the number of signal events (S_{exp}^{95}) given the expected number of background events (and $\pm 1\sigma$ excursions of the expectation).

The results of the searches for gluino-pair production with a one-step decay via an intermediate chargino into $qqW\tilde{\chi}_1^0$ are shown in Figure 15. Figure 15(a) shows the limit for a chargino mass chosen as $m(\tilde{\chi}_1^\pm) = (m(\tilde{g}) + m(\tilde{\chi}_1^0))/2$. In the region close to the kinematic limit near the diagonal, neutralino and gluino masses up to 900 GeV are excluded, as obtained by the multi-bin signal regions dedicated to models with compressed mass spectra. For massless neutralino, gluino masses are excluded below 2190 GeV. Fixing the neutralino mass at 60 GeV (Figure 15(b)), one obtains limits on the variable $x = \Delta m(\tilde{\chi}_1^\pm, \tilde{\chi}_1^0)/\Delta m(\tilde{g}, \tilde{\chi}_1^0)$. Gluino masses are excluded up to 2150 GeV for the most favourable x values.

Figure 16 expresses the mass limits in the $(m(\tilde{g}), m(\tilde{q}))$ plane in the model with combined production of squark pairs, gluino pairs, and of squark–gluino pairs, for different assumptions on the neutralino mass:

Model independent regions					
Signal Region	SR-2j-1600	SR-2j-2200	SR-2j-2800	SR-4j-1000	SR-4j-2200
Fitted background events					
Diboson	130 ± 29	74 ± 17	5.8 ± 1.7	44 ± 12	6.3 ± 1.7
Z/ γ^* +jets	1510 ± 120	670 ± 40	64 ± 7	282 ± 22	35 ± 4
W+jets	500 ± 50	225 ± 16	15.4 ± 2.4	144 ± 12	15.4 ± 1.9
$t\bar{t}$ (+EW) + single top	44 ± 9	14 ± 4	1.4 ± 0.8	67 ± 14	2.4 ± 0.9
Multi-jet	0.22 ± 0.22	0.32 ± 0.32	—	0.17 ± 0.17	$0.03^{+0.03}_{-0.03}$
Total bkg (pre-fit)	2120	979	82	610	71
Total bkg	2190 ± 130	980 ± 50	87 ± 8	536 ± 31	60 ± 5
Observed	2111	971	78	535	60
$\langle\epsilon\sigma\rangle_{obs}^{95}$ [fb]	1.46	0.78	0.13	0.54	0.14
S_{obs}^{95}	204	108	19	75	19
S_{exp}^{95}	246^{+91}_{-67}	114^{+43}_{-31}	24^{+10}_{-7}	76^{+27}_{-23}	19^{+8}_{-5}
p_0 (Z)	0.50 (0.00)	0.50 (0.00)	0.50 (0.00)	0.50 (0.00)	0.50 (0.00)
Signal Region	SR-4j-3400	SR-5j-1600	SR-6j-1000	SR-6j-2200	SR-6j-3400
Fitted background events					
Diboson	0.74 ± 0.24	36 ± 9	1.8 ± 0.6	$0.33^{+0.80}_{-0.33}$	0.07 ± 0.02
Z/ γ^* +jets	3.3 ± 0.8	170 ± 16	9.3 ± 1.8	2.4 ± 0.6	0.32 ± 0.19
W+jets	1.6 ± 0.4	80 ± 7	7.2 ± 1.6	1.6 ± 0.5	0.41 ± 0.31
$t\bar{t}$ (+EW) + single top	$0.09^{+0.12}_{-0.09}$	33 ± 6	2.7 ± 1.5	0.38 ± 0.3	$0.03^{+0.04}_{-0.03}$
Multi-jet	$0.05^{+0.05}_{-0.05}$	0.23 ± 0.23	—	—	—
Total bkg (pre-fit)	6.5	427	29	7.0	1.1
Total bkg	5.7 ± 1.0	319 ± 19	21.0 ± 2.9	4.6 ± 1.0	0.8 ± 0.4
Observed	4	320	25	5	0
$\langle\epsilon\sigma\rangle_{obs}^{95}$ [fb]	0.04	0.36	0.11	0.04	0.02
S_{obs}^{95}	5	50	15	6	3
S_{exp}^{95}	$6.1^{+2.9}_{-1.2}$	50^{+11}_{-13}	12^{+5}_{-4}	$5.8^{+2.8}_{-1.3}$	$3.0^{+1.2}_{-0.1}$
p_0 (Z)	0.50 (0.00)	0.48 (0.05)	0.24 (0.71)	0.48 (0.04)	0.50 (0.00)

Table 12: Numbers of events observed in the signal regions used in the model-independent search, compared with background expectations obtained from the fits described in the text and from the MC expectations. Empty cells (indicated by a ‘—’) correspond to estimates lower than 0.01. The p-values (p_0) give the probabilities of the observations being consistent with the estimated backgrounds. For an observed number of events lower than expected, the p-value is truncated at 0.5. Between parentheses, p-values are also given as the number of equivalent Gaussian standard deviations (Z). Also shown are 95% CL upper limits on the visible cross-section ($\langle\epsilon\sigma\rangle_{obs}^{95}$), the visible number of signal events (S_{obs}^{95}) and the number of signal events (S_{exp}^{95}) given the expected number of background events (and $\pm 1\sigma$ excursions of the expectation).

$m(\tilde{\chi}_1^0) = 0$ GeV, 995 GeV or 1495 GeV. Depending on the mass hierarchy, the $\tilde{g} \rightarrow \tilde{q}q$ and $\tilde{q} \rightarrow \tilde{g}q$ one-step decays are taken into account. The masses of all other supersymmetric particles are set outside the kinematic reach. A lower limit of 3000 GeV for equal squark and gluino mass is found for the scenario with a massless $\tilde{\chi}_1^0$.

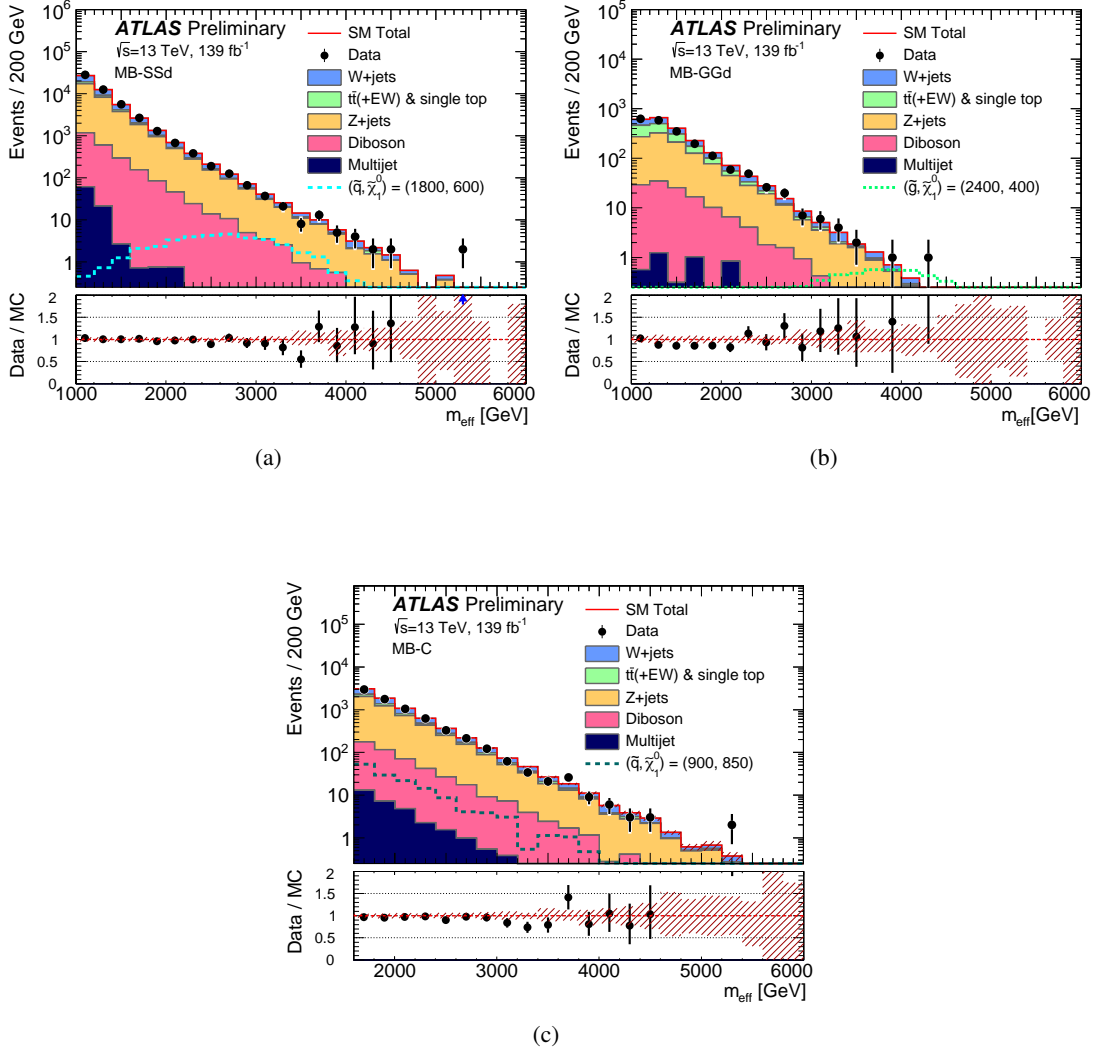


Figure 8: Observed m_{eff} distributions for the (a) MB-SSd, (b) MB-GGd and (c) MB-C regions obtained after applying the selection criteria from Table 3, before the final binning selections on this quantity. The histograms show the MC background predictions prior to the fits described in the text, normalized to the cross-section times integrated luminosity. The hatched (red) error bands indicate the combined experimental and MC statistical uncertainties. Expected distributions for benchmark signal model points, normalized using NLO+NLL cross-section (Section 3) times integrated luminosity, are also shown for comparison (masses in GeV).

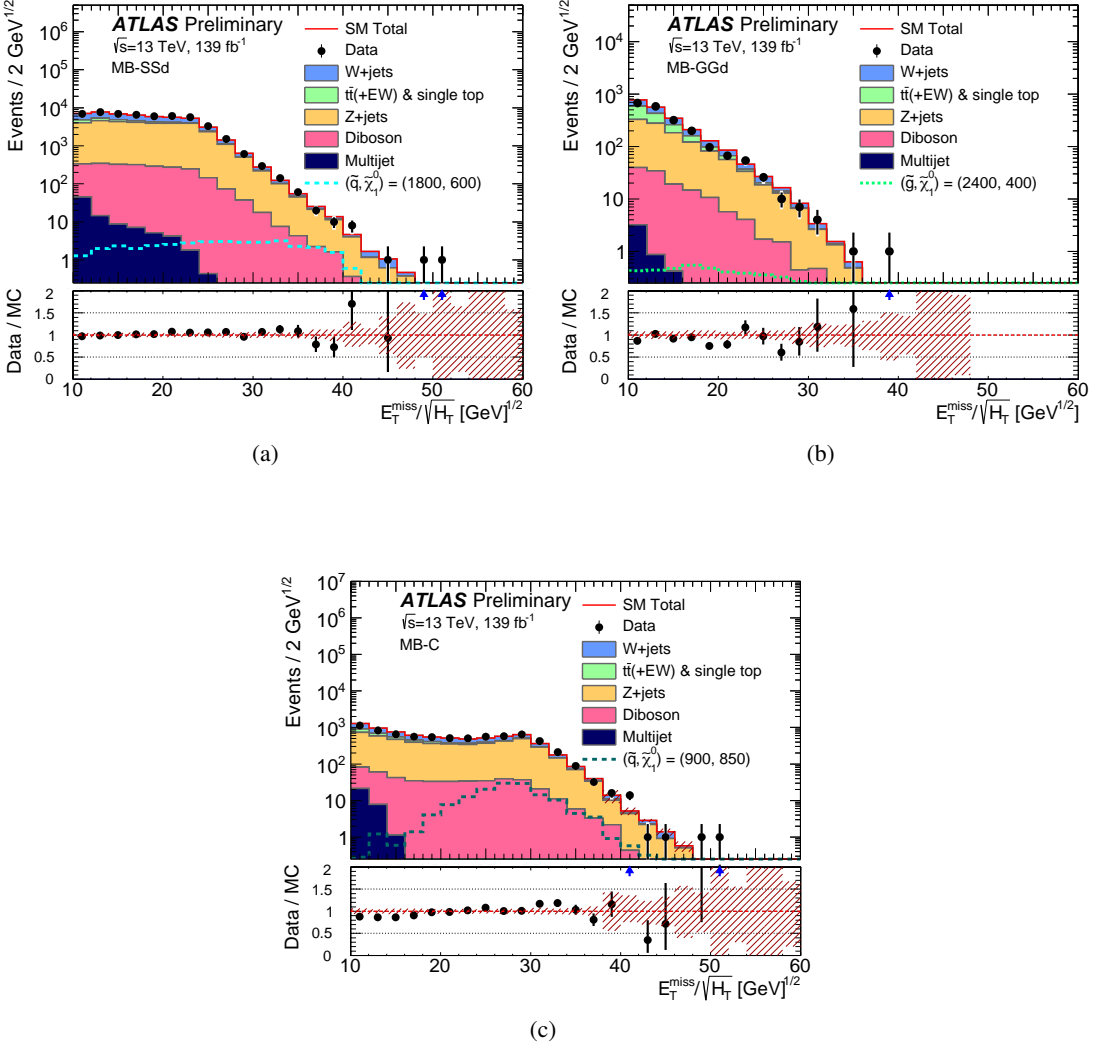


Figure 9: Observed $E_T^{\text{miss}} / \sqrt{H_T}$ distributions for the (a) MB-SSd, (b) MB-GGd and (c) MB-C regions obtained after applying the selection criteria from Table 3, before the final binning selections on this quantity. The histograms show the MC background predictions prior to the fits described in the text, normalized to the cross-section times integrated luminosity. The hatched (red) error bands indicate the combined experimental and MC statistical uncertainties. Expected distributions for benchmark signal model points, normalized using NLO+NLL cross-section (Section 3) times integrated luminosity, are also shown for comparison (masses in GeV).

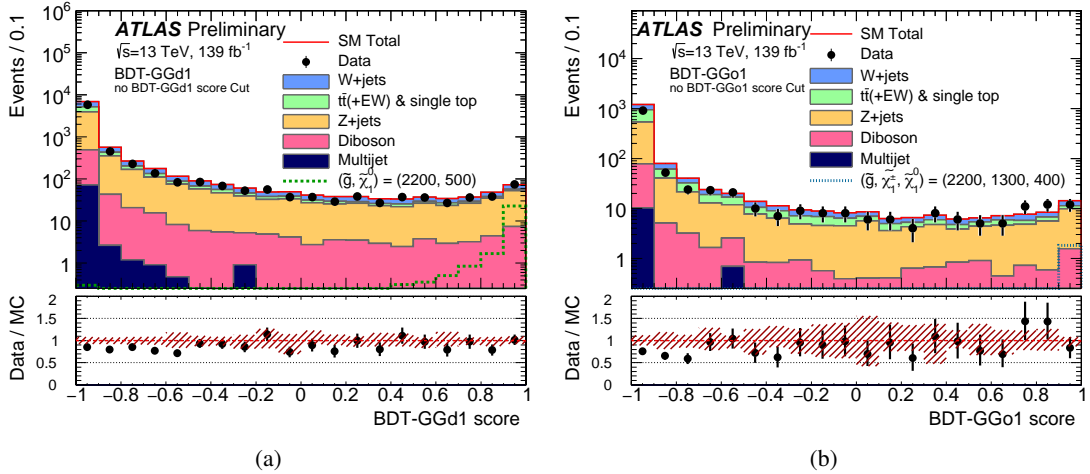


Figure 10: Observed BDT score distributions for the (a) BDT-GGd1 and (b) BDT-GGo1 regions obtained after applying the selection criteria from Table 7. The histograms show the MC background predictions prior to the fits described in the text, normalized to the cross-section times integrated luminosity. The hatched (red) error bands indicate the combined experimental and MC statistical uncertainties. Expected distributions for benchmark signal model points, normalized using NLO+NLL cross-section (Section 3) times integrated luminosity, are also shown for comparison (masses in GeV).

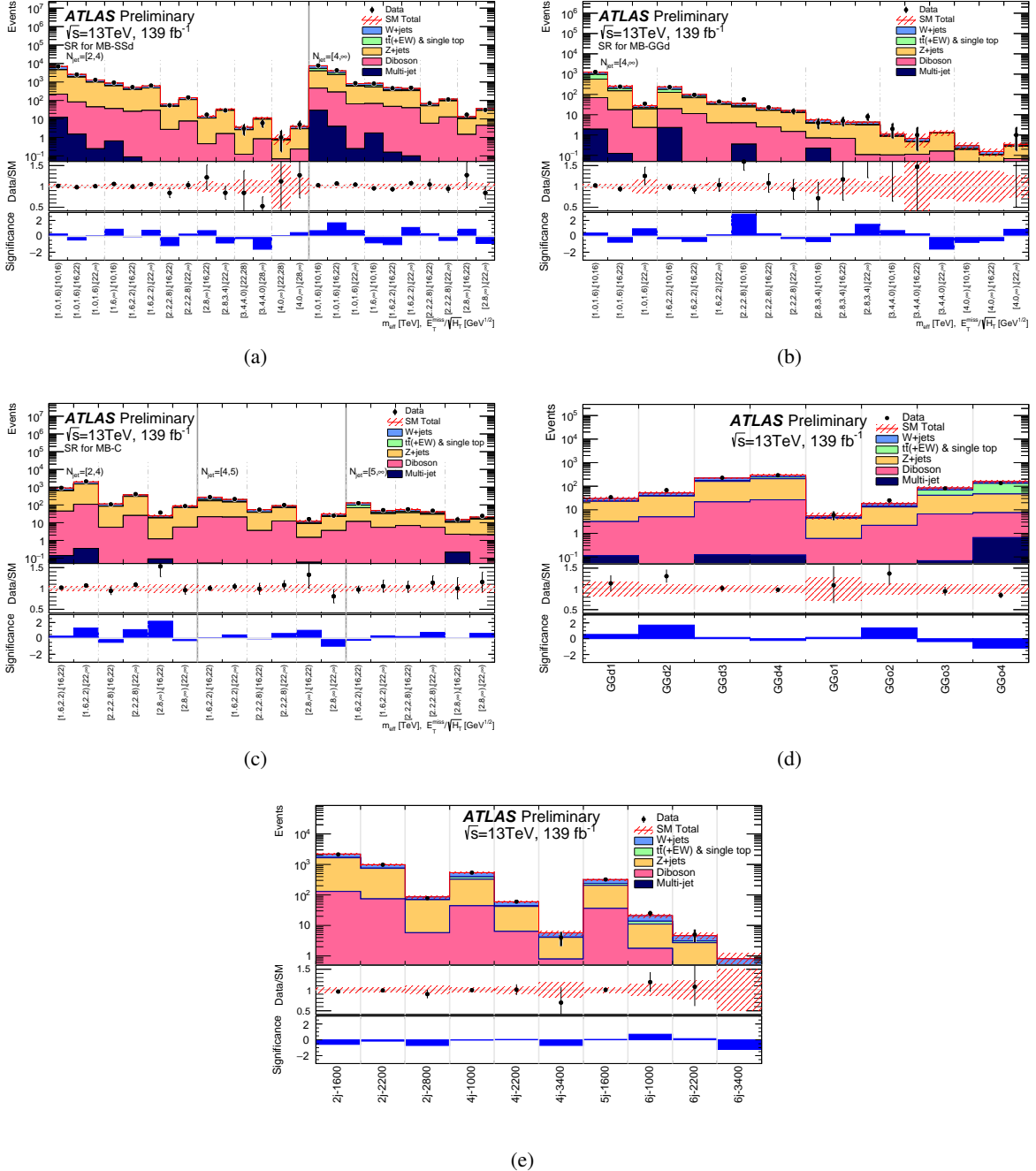


Figure 11: Comparison of the observed and expected event yields as a function of signal region in the (a) MB-SSd, (b) MB-GGd, (c) MB-C regions from the multi-bin, (d) regions from the BDT search, and (e) regions from the model-independent search. The background predictions are those obtained from the background-only fits, as explained in the text. The significance is computed following the profile likelihood method of Ref. [83] in the case where the observed yield exceeds the prediction, and using the same expression with an overall minus sign if the yield is below the prediction. The hatched (red) error bands indicate the combined experimental and MC statistical uncertainties.

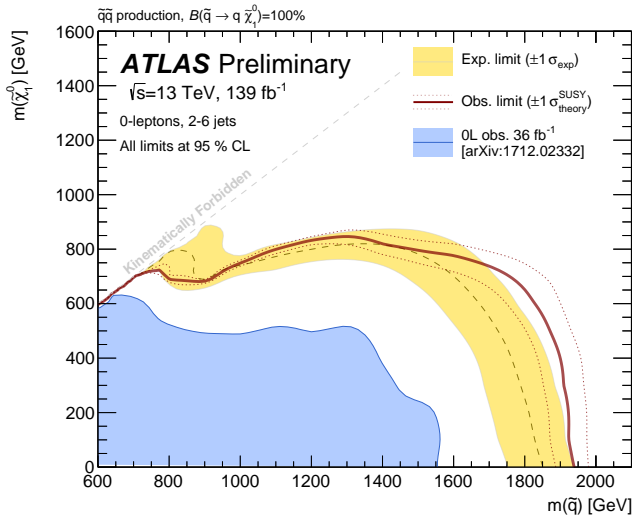


Figure 12: Exclusion limits in the mass plane of the lightest neutralino and first- and second-generation squarks assuming squark-pair production and direct decays $\tilde{q} \rightarrow q \tilde{\chi}_1^0$ obtained by using the signal region from the optimized multi-bin search with the best expected sensitivity at each point. The blue dashed lines show the expected limits at 95% CL, with the light (yellow) bands indicating the 1σ excursions due to experimental and background-only theoretical uncertainties. Observed limits are indicated by medium dark (maroon) curves where the solid contour represents the nominal limit, and the dotted lines are obtained by varying the signal cross-section by the renormalization and factorization scale and PDF uncertainties. Results are compared with the observed limits obtained by the previous ATLAS searches with jets, missing transverse momentum, and no leptons [13].

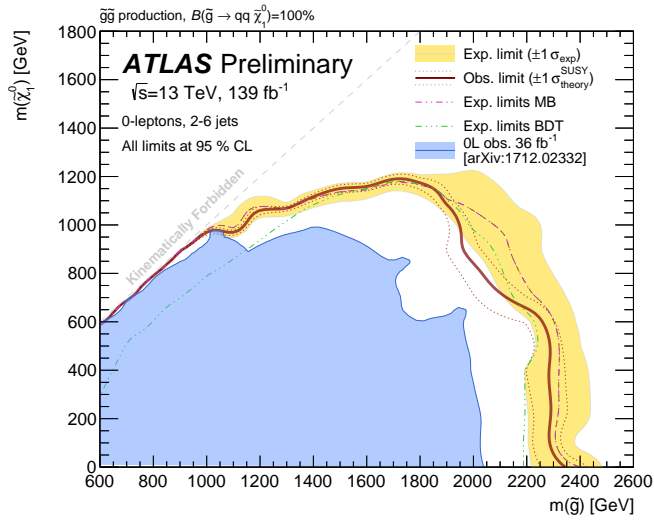


Figure 13: Exclusion limits in the mass plane of the lightest neutralino and the gluino for gluino-pair production with direct decay $\tilde{g} \rightarrow qq\tilde{\chi}_1^0$ obtained by using the signal region with the best expected sensitivity at each point. Expected limits from the multi-bin (MB) and BDT searches are also shown for comparison, with the light (yellow) bands indicating the $\pm 1\sigma$ ranges of the expected fluctuations around the expected limit due to experimental and background-only theoretical uncertainties. Observed limits are indicated by medium dark (maroon) curves where the solid contour represents the nominal limit, and the dotted lines are obtained by varying the signal cross-section by the renormalization and factorization scale and PDF uncertainties. Results are compared with the observed limits obtained by the previous ATLAS searches with jets, missing transverse momentum, and no leptons [13].

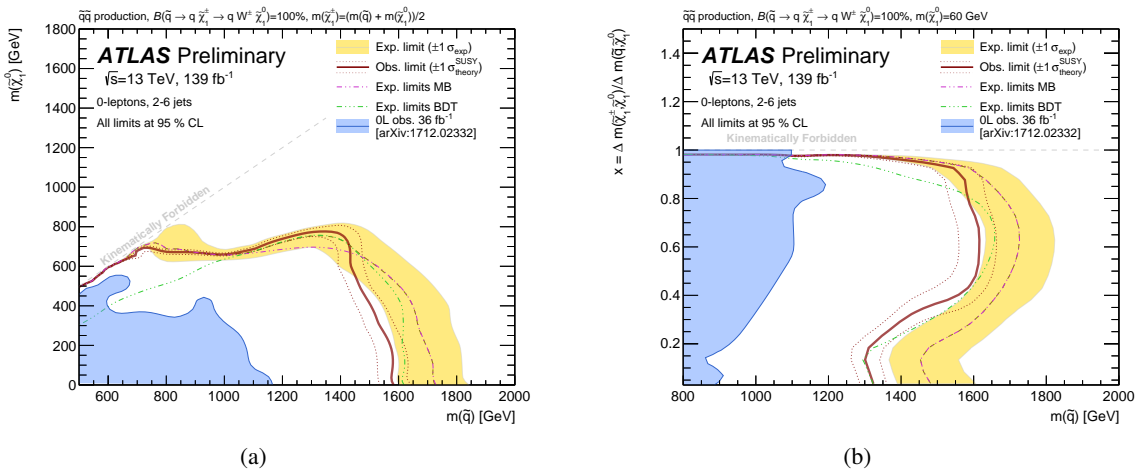


Figure 14: Exclusion limits for squark-pair production with a one-step decay via an intermediate chargino into $qW\tilde{\chi}_1^0$. Figure (a) shows the limits in the $(m(\tilde{q}), m(\tilde{\chi}_1^0))$ plane for a chargino mass fixed at $m(\tilde{\chi}_1^\pm) = (m(\tilde{q}) + m(\tilde{\chi}_1^0))/2$. Alternatively in Figure (b), the neutralino mass is fixed at 60 GeV and exclusion limits are given for $x = \Delta m(\tilde{\chi}_1^\pm, \tilde{\chi}_1^0) / \Delta m(\tilde{q}, \tilde{\chi}_1^0)$ as function of the squark mass. Exclusion limits are obtained by using the signal region with the best expected sensitivity at each point. Expected limits from the multi-bin (MB) and BDT searches are also shown for comparison, with the light (yellow) bands indicating the $\pm 1\sigma$ ranges of the expected fluctuations around the expected limit due to experimental and background-only theoretical uncertainties. Observed limits are indicated by medium dark (maroon) curves where the solid contour represents the nominal limit, and the dotted lines are obtained by varying the signal cross-section by the renormalization and factorization scale and PDF uncertainties. Results are compared with the observed limits obtained by the previous ATLAS searches with jets, missing transverse momentum, and no leptons [13].

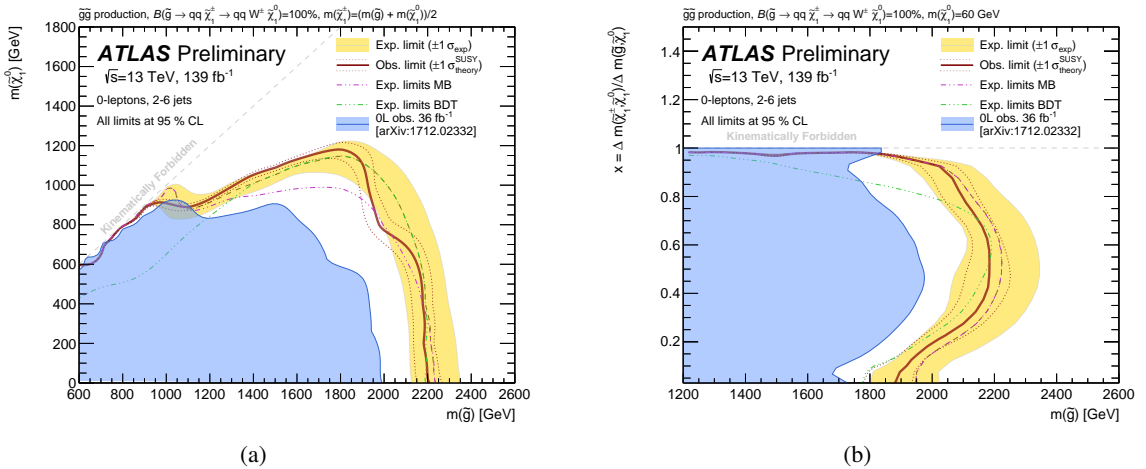


Figure 15: Exclusion limits for gluino-pair production with a one-step decay via an intermediate chargino into $q\bar{q}W\tilde{\chi}_1^0$. Figure (a) shows the limits in the $(m(\tilde{g}), m(\tilde{\chi}_1^0))$ plane for a chargino mass fixed at $m(\tilde{\chi}_1^\pm) = (m(\tilde{g}) + m(\tilde{\chi}_1^0))/2$. Alternatively in Figure (b), the neutralino mass is fixed at 60 GeV and exclusion limits are given for $x = \Delta m(\tilde{\chi}_1^\pm, \tilde{\chi}_1^0) / \Delta m(\tilde{g}, \tilde{\chi}_1^0)$ as function of the gluino mass. Exclusion limits are obtained by using the signal region with the best expected sensitivity at each point. Expected limits from the multi-bin (MB) and BDT searches are also shown for comparison, with the light (yellow) bands indicating the $\pm 1\sigma$ ranges of the expected fluctuations around the expected limit due to experimental and background-only theoretical uncertainties. Observed limits are indicated by medium dark (maroon) curves where the solid contour represents the nominal limit, and the dotted lines are obtained by varying the signal cross-section by the renormalization and factorization scale and PDF uncertainties. Results are compared with the observed limits obtained by the previous ATLAS searches with jets, missing transverse momentum, and no leptons [13].

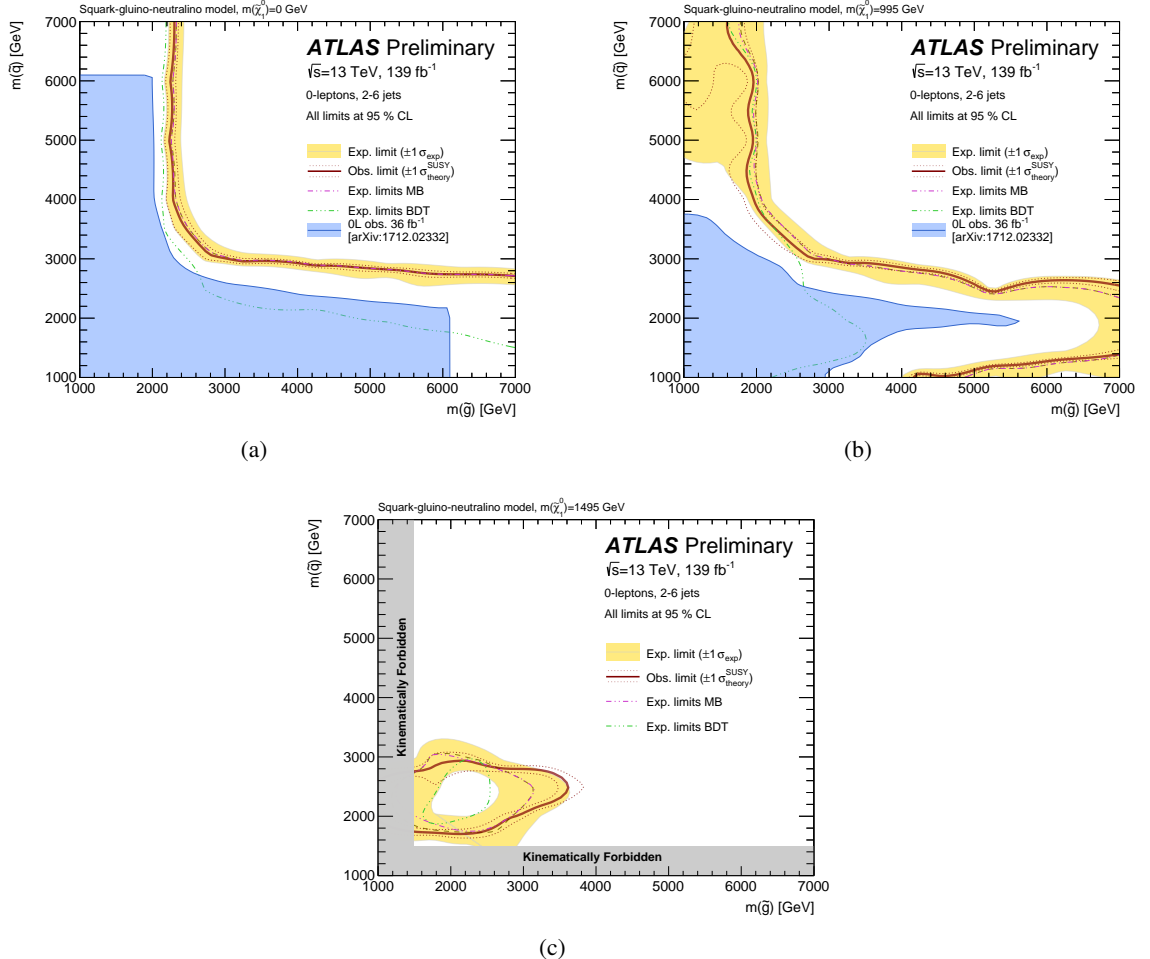


Figure 16: Exclusion limits for the model with combined production of squark pairs, gluino pairs, and of squark–gluino pairs, for different assumptions on the neutralino mass: (a) $m(\tilde{\chi}_1^0) = 0$ GeV, (b) $m(\tilde{\chi}_1^0) = 995$ GeV and (c) $m(\tilde{\chi}_1^0) = 1495$ GeV varying values of $m(\tilde{g})$ and $m(\tilde{q})$ and assuming purely bino $\tilde{\chi}_1^0$. Exclusion limits are obtained by using the signal region with the best expected sensitivity at each point. Expected limits from the multi-bin (MB) and BDT searches are also shown for comparison, with the light (yellow) bands indicating the $\pm 1\sigma$ ranges of the expected fluctuations around the expected limit due to experimental and background-only theoretical uncertainties. Observed limits are indicated by medium dark (maroon) curves where the solid contour represents the nominal limit, and the dotted lines are obtained by varying the signal cross-section by the renormalization and factorization scale and PDF uncertainties. Results (a,b) are compared with the observed limits obtained by the previous ATLAS searches with no leptons, jets and missing transverse momentum [13].

9 Conclusions

This document presents the results of two searches for squarks and gluinos in final states containing high- p_T jets, large missing transverse momentum but no electrons or muons, based on a 139 fb^{-1} dataset of $\sqrt{s} = 13 \text{ TeV}$ proton–proton collisions recorded by the ATLAS experiment at the LHC. No significant deviation from the background expectation is found.

Results are interpreted in terms of simplified models with only first- and second-generation squarks, or gluinos, together with a neutralino LSP, with the masses of all the other SUSY particles set such that the particles are effectively decoupled. For a massless lightest neutralino, gluino masses below 2.35 TeV are excluded at the 95% confidence level in a simplified model with only gluinos and the lightest neutralino. For a simplified model involving the strong production of squarks of the first and second generations, with decays to a massless lightest neutralino, squark masses below 1.94 TeV are excluded, assuming mass-degenerate squarks of the first two generations. In simplified models with pair-produced squarks and gluinos, each decaying via an intermediate $\tilde{\chi}_1^\pm$ to one quark or two quarks, a W boson and a $\tilde{\chi}_1^0$, squark masses below 1.59 TeV and gluino masses below 2.19 TeV are excluded for massless $\tilde{\chi}_1^0$. In models with combined production of squark pairs, gluino pairs, and of squark-gluino pairs, a lower limit of 3000 GeV for equal squark and gluino mass is found for the scenario with a massless $\tilde{\chi}_1^0$.

These results substantially extend the region of supersymmetric parameter space previously excluded by similar ATLAS searches.

A Observed and expected event yields for the multi-bin search

Signal Region	MB-SSd regions							
	2-1000-10	2-1000-16	2-1000-22	2-1600-10	2-1600-16	2-1600-22	2-2200-16	2-2200-22
Fitted background events								
Diboson	210 \pm 50	81 \pm 18	44 \pm 10	36 \pm 8	26 \pm 6	29 \pm 7	2.7 \pm 0.7	7.6 \pm 2.2
Z/γ^* +jets	4360 \pm 280	1760 \pm 90	930 \pm 50	580 \pm 40	366 \pm 25	443 \pm 28	45.1 \pm 3.5	104 \pm 7
W +jets	2178 \pm 100	702 \pm 25	294 \pm 9	245 \pm 13	131 \pm 6	131 \pm 5	16.1 \pm 0.8	29.2 \pm 1.3
$t\bar{t}$ (+EW) + single top	133 \pm 28	48 \pm 10	16 \pm 4	11.3 \pm 2.3	5.2 \pm 1.4	5 \pm 4	1.3 \pm 1.0	1.51 $^{+1.74}_{-1.51}$
Multi-jet	12 \pm 12	1.5 \pm 1.5	0.24 \pm 0.24	0.7 \pm 0.6	0.09 \pm 0.09	0.02 \pm 0.02	0.01 \pm 0.1	0.02 \pm 0.02
Total bkg (pre-fit)	6570.36	2424.38	1201.77	851.26	509.44	575.91	62.24	135.99
Total bkg	6890 \pm 300	2589 \pm 100	1290 \pm 50	870 \pm 50	528 \pm 27	608 \pm 30	65 \pm 4	142 \pm 8
Observed	6986	2537	1289	926	526	638	55	146
Signal Region	2-2800-16	2-2800-22	2-3400-22	2-3400-28	2-4000-22	2-4000-28	4-1000-10	4-1000-16
Fitted background events								
Diboson	0.45 \pm 0.14	1.6 \pm 0.8	0.12 \pm 0.04	0.83 $^{+0.85}_{-0.83}$	0.07 \pm 0.03	0.23 \pm 0.1	432 \pm 22	282 \pm 18
Z/γ^* +jets	10.6 \pm 1.4	27.3 \pm 2.6	2.47 \pm 0.34	8.8 \pm 1.1	0.65 \pm 0.29	2.7 \pm 0.5	3520 \pm 240	2210 \pm 140
W +jets	2.8 \pm 0.4	5.4 \pm 0.4	0.9 \pm 0.4	1.6 \pm 0.4	0.08 \pm 0.06	1.0 \pm 0.4	2119 \pm 100	970 \pm 50
$t\bar{t}$ (+EW) + single top	0.09 $^{+0.13}_{-0.09}$	0.03 $^{+0.05}_{-0.03}$	0.01 \pm 0.1	0.18 $^{+0.44}_{-0.18}$	0.10 $^{+0.27}_{-0.10}$	–	1470 \pm 90	550 \pm 50
Multi-jet	–	–	–	–	–	–	29 \pm 29	4 \pm 4
Total bkg (pre-fit)	13.68	33.89	3.30	11.18	1.16	3.93	8467.25	4486.63
Total bkg	14.0 \pm 1.5	34.3 \pm 2.8	3.5 \pm 0.6	11.4 \pm 1.6	0.9 \pm 0.5	4.0 \pm 0.8	7570 \pm 260	4010 \pm 140
Observed	17	29	3	6	1	5	7769	4286
Signal Region	4-1000-22	4-1600-10	4-1600-16	4-1600-22	4-2200-16	4-2200-22	2-2800-16	2-2800-22
Fitted background events								
Diboson	65 \pm 4	66 \pm 17	48 \pm 12	40 \pm 10	5.8 \pm 1.7	12.7 \pm 3.4	0.45 \pm 0.14	1.6 \pm 0.8
Z/γ^* +jets	528 \pm 30	466 \pm 32	290 \pm 19	299 \pm 18	45.1 \pm 3.2	82 \pm 5	10.6 \pm 1.4	27.3 \pm 2.6
W +jets	174 \pm 13	224 \pm 9	114 \pm 7	87 \pm 4	14.2 \pm 1.0	21.3 \pm 1.1	2.8 \pm 0.4	5.4 \pm 0.4
$t\bar{t}$ (+EW) + single top	55 \pm 15	101 \pm 14	43 \pm 5	24 \pm 6	2.8 \pm 0.5	3.4 \pm 1.4	0.09 $^{+0.13}_{-0.09}$	0.03 $^{+0.05}_{-0.03}$
Multi-jet	0.24 \pm 0.24	1.7 \pm 1.7	0.16 \pm 0.16	0.1 \pm 0.1	0.02 \pm 0.02	0.05 \pm 0.05	–	–
Total bkg (pre-fit)	899.55	982.49	556.41	511.78	78.64	135.43	13.68	33.89
Total bkg	820 \pm 40	860 \pm 40	494 \pm 23	450 \pm 22	68 \pm 4	120 \pm 7	14.0 \pm 1.5	34.3 \pm 2.8
Observed	858	819	461	485	71	113	17	29

Table 13: Numbers of events observed in the signal regions used in the multi-bin search regions targeting squark-pair production followed by the direct decay of \tilde{q} , compared with background expectations obtained from the fits described in the text. The errors include all sources of statistical and systematic uncertainty described in Section 7. Empty cells (indicated by a ‘–’) correspond to estimates lower than 0.01 events.

MB-GGd regions						
Signal Region	4-1000-10	4-1000-16	4-1000-22	4-1600-10	4-1600-16	4-1600-22
Fitted background events						
Diboson	67 ± 18	17 ± 5	2.3 ± 0.8	17 ± 5	11.4 ± 2.9	4.0 ± 1.5
Z/γ^* +jets	500 ± 40	132 ± 10	16.9 ± 1.7	107 ± 9	57 ± 4	28.2 ± 2.6
W +jets	296 ± 25	60 ± 5	6.1 ± 1.3	59 ± 5	22.9 ± 2.0	8.3 ± 0.8
$t\bar{t}$ (+EW) + single top	391 ± 24	46 ± 7	$2.68^{+3.56}_{-2.68}$	49 ± 5	11.3 ± 2.2	2.1 ± 1.6
Multi-jet	1.9 ± 1.9	0.12 ± 0.12	0.01 ± 0.1	2.3 ± 2.3	–	0.02 ± 0.02
Total bkg (pre-fit)	1365.21	279.03	29.97	266.07	114.40	47.23
Total bkg	1250 ± 50	256 ± 14	28 ± 5	234 ± 13	102 ± 6	43 ± 4
Observed	1281	240	35	228	95	44
Signal Region	4-2200-10	4-2200-16	4-2200-22	4-2800-10	4-2800-16	4-2800-22
Fitted background events						
Diboson	2.5 ± 1.0	2.5 ± 1.0	1.5 ± 0.5	0.68 ± 0.24	0.68 ± 0.24	0.11 ± 0.1
Z/γ^* +jets	13.7 ± 1.2	13.7 ± 1.2	11.2 ± 1.3	2.6 ± 0.5	2.6 ± 0.5	3.0 ± 0.4
W +jets	4.4 ± 0.6	4.4 ± 0.6	3.23 ± 0.32	0.87 ± 0.21	0.87 ± 0.21	1.1 ± 0.15
$t\bar{t}$ (+EW) + single top	0.74 ± 0.19	0.74 ± 0.19	0.24 ± 0.15	0.1 ± 0.09	0.1 ± 0.09	0.13 ± 0.07
Multi-jet	–	–	–	–	–	–
Total bkg (pre-fit)	24.74	24.74	18.85	5.01	5.01	5.33
Total bkg	21.3 ± 1.6	21.3 ± 1.6	16.2 ± 1.6	4.3 ± 0.8	4.3 ± 0.8	4.3 ± 0.5
Observed	23	23	15	5	5	8
Signal Region	4-3400-10	4-3400-16	4-3400-22	4-4000-10	4-4000-16	4-4000-22
Fitted background events						
Diboson	$0.11^{+0.23}_{-0.11}$	$0.11^{+0.23}_{-0.11}$	0.16 ± 0.13	–	–	0.07 ± 0.1
Z/γ^* +jets	0.35 ± 0.27	0.35 ± 0.27	1.09 ± 0.3	0.07 ± 0.03	0.07 ± 0.03	0.21 ± 0.06
W +jets	0.21 ± 0.12	0.21 ± 0.12	$0.12^{+0.17}_{-0.12}$	0.05 ± 0.1	0.05 ± 0.1	0.06 ± 0.02
$t\bar{t}$ (+EW) + single top	$0.01^{+0.01}_{-0.01}$	$0.01^{+0.01}_{-0.01}$	$0.00^{+0.00}_{-0.00}$	$0.00^{+0.00}_{-0.00}$	$0.00^{+0.00}_{-0.00}$	$0.00^{+0.03}_{-0.00}$
Multi-jet	–	–	–	$0.04^{+0.04}_{-0.04}$	$0.04^{+0.04}_{-0.04}$	–
Total bkg (pre-fit)	0.92	0.92	1.52	0.14	0.14	0.39
Total bkg	0.7 ± 0.4	0.7 ± 0.4	1.4 ± 0.4	0.15 ± 0.06	0.15 ± 0.06	0.34 ± 0.09
Observed	1	1	0	0	0	1

Table 14: Numbers of events observed in the signal regions used in the multi-bin search regions targeting the production of gluino-pairs followed by the direct decay of \tilde{g} , compared with background expectations obtained from the fits described in the text. The errors include all sources of statistical and systematic uncertainty described in Section 7. Empty cells (indicated by a ‘–’) correspond to estimates lower than 0.01 events.

MB-C regions						
Signal Region	2-1600-16	2-1600-22	2-2200-16	2-2200-22	2-2800-16	2-2800-22
Fitted background events						
Diboson	45 \pm 10	108 \pm 22	5.5 \pm 1.4	25 \pm 6	1.1 \pm 0.4	5.6 \pm 1.6
Z/γ^* +jets	580 \pm 50	1400 \pm 90	78 \pm 7	274 \pm 21	17.2 \pm 2.0	65 \pm 7
W +jets	239 \pm 13	429 \pm 19	28.5 \pm 1.8	71 \pm 4	5.7 \pm 0.6	17.8 \pm 1.7
$t\bar{t}$ (+EW) + single top	22.6 \pm 3.4	33 \pm 9	1.0 \pm 0.8	2.3 \pm 1.0	0.07 ^{+0.28} _{-0.07}	0.06 ^{+0.21} _{-0.06}
Multi-jet	0.14 \pm 0.14	0.35 \pm 0.35	0.01 \pm 0.1	0.05 \pm 0.05	0.09 ^{+0.09} _{-0.09}	0.02 ^{+0.02} _{-0.02}
Total bkg (pre-fit)	867.04	1908.27	109.06	360.02	23.89	86.02
Total bkg	890 \pm 50	1969 \pm 100	113 \pm 7	373 \pm 22	24.2 \pm 2.3	89 \pm 8
Observed	908	2108	107	406	37	85
Signal Region	4-1600-16	4-1600-22	4-2200-16	4-2200-22	4-2800-16	4-2800-22
Fitted background events						
Diboson	21 \pm 6	21 \pm 5	3.6 \pm 1.0	12 \pm 4	1.4 \pm 0.5	3.6 \pm 1.0
Z/γ^* +jets	148 \pm 15	125 \pm 12	34 \pm 4	57 \pm 5	7.5 \pm 0.9	18.6 \pm 1.9
W +jets	71 \pm 5	47 \pm 4	14.9 \pm 0.9	18.3 \pm 1.5	2.74 \pm 0.27	6.7 \pm 0.8
$t\bar{t}$ (+EW) + single top	32.1 \pm 3.0	12.1 \pm 1.8	1.7 \pm 0.6	2.6 \pm 0.9	0.37 \pm 0.17	1.9 \pm 1.1
Multi-jet	0.05 \pm 0.05	0.04 \pm 0.04	0.03 \pm 0.03	0.03 \pm 0.03	0.06 ^{+0.06} _{-0.06}	–
Total bkg (pre-fit)	323.81	248.05	64.73	103.69	13.60	34.22
Total bkg	273 \pm 17	204 \pm 15	54 \pm 4	91 \pm 7	12.0 \pm 1.2	30.8 \pm 2.7
Observed	274	213	54	98	16	25
Signal Region	5-1600-16	5-1600-22	5-2200-16	5-2200-22	5-2800-16	5-2800-22
Fitted background events						
Diboson	11.6 \pm 3.0	5.4 \pm 1.4	6.8 \pm 1.9	5.5 \pm 1.7	2.0 \pm 0.5	2.1 \pm 0.8
Z/γ^* +jets	58 \pm 6	26.8 \pm 2.7	29.4 \pm 3.5	24.1 \pm 2.5	8.2 \pm 0.9	13.8 \pm 1.4
W +jets	32.5 \pm 2.5	11.7 \pm 1.0	12.7 \pm 0.9	8.2 \pm 0.7	3.5 \pm 0.4	3.8 \pm 0.4
$t\bar{t}$ (+EW) + single top	27.4 \pm 2.7	4.4 \pm 1.1	5.9 \pm 0.9	3.6 \pm 0.7	1.06 \pm 0.27	1.15 \pm 0.32
Multi-jet	0.04 ^{+0.04} _{-0.04}	–	0.04 \pm 0.04	0.02 \pm 0.02	0.21 ^{+0.21} _{-0.21}	–
Total bkg (pre-fit)	176.28	67.04	74.09	59.02	20.62	30.13
Total bkg	129 \pm 8	48 \pm 4	55 \pm 4	41.3 \pm 3.4	15.0 \pm 1.4	20.8 \pm 1.9
Observed	126	51	57	47	15	24

Table 15: Numbers of events observed in the signal regions used in the multi-bin search regions targeting gluino- or squark-pair production in models with compressed mass spectra, compared with background expectations obtained from the fits described in the text. The errors include all sources of statistical and systematic uncertainty described in Section 7. Empty cells (indicated by a ‘–’) correspond to estimates lower than 0.01 events.

B Cut-flow tables

	Selection	$m(\tilde{q}) = 1200 \text{ GeV}$, $m(\tilde{\chi}_1^0) = 600 \text{ GeV}$	$m(\tilde{q}) = 1400 \text{ GeV}$, $m(\tilde{\chi}_1^0) = 600 \text{ GeV}$	$m(\tilde{q}) = 1600 \text{ GeV}$, $m(\tilde{\chi}_1^0) = 400 \text{ GeV}$
Generated MC events		10000	6000	6000
Common Requirements	Pre-selection, $E_T^{\text{miss}} > 300 \text{ GeV}$, $p_T(\text{jet}_1) > 200 \text{ GeV}$, $m_{\text{eff}} > 800 \text{ GeV}$	1763	541	174
	jet multiplicity ≥ 2	1763	541	174
	Cleaning Cuts	1746	535	173
SR2j-1600	$\Delta\phi(\text{jet}_{1,2,(3)}, \mathbf{p}_T^{\text{miss}})_{\text{min}} > 0.8$	1433	431	136
	$\Delta\phi(\text{jet}_{i>3}, \mathbf{p}_T^{\text{miss}})_{\text{min}} > 0.4$	1377	411	129
	$p_T(\text{jet}_2) > 250 \text{ GeV}$	853	311	111
	$ \eta(j_{1,2}) < 2.0$	836	306	109
	$E_T^{\text{miss}}/\sqrt{H_T} > 16 \text{ GeV}^{1/2}$	568	228	86.4
	$m_{\text{eff}} > 1600 \text{ GeV}$	366	202	83.5
SR2j-2200	$\Delta\phi(\text{jet}_{1,2,(3)}, \mathbf{p}_T^{\text{miss}})_{\text{min}} > 0.4$	1603	483	156
	$\Delta\phi(\text{jet}_{i>3}, \mathbf{p}_T^{\text{miss}})_{\text{min}} > 0.2$	1567	470	151
	$p_T(\text{jet}_1) > 600 \text{ GeV}$	509	269	120
	$E_T^{\text{miss}}/\sqrt{H_T} > 16 \text{ GeV}^{1/2}$	337	201	94.6
	$m_{\text{eff}} > 2200 \text{ GeV}$	101	108	76.1
SR2j-2800	$\Delta\phi(\text{jet}_{1,2,(3)}, \mathbf{p}_T^{\text{miss}})_{\text{min}} > 0.8$	1433	431	136
	$\Delta\phi(\text{jet}_{i>3}, \mathbf{p}_T^{\text{miss}})_{\text{min}} > 0.4$	1377	411	129
	$p_T(\text{jet}_2) > 250 \text{ GeV}$	853	311	111
	$ \eta(j_{1,2}) < 1.2$	655	235	82.3
	$E_T^{\text{miss}}/\sqrt{H_T} > 16 \text{ GeV}^{1/2}$	439	173	64.6
	$m_{\text{eff}} > 2800 \text{ GeV}$	15.6	18.8	29.1

Table 16: Cut-flow for model-independent search regions targeting squarks for SS direct model points. Expected yields are normalized to a luminosity of 139 fb^{-1} .

	Selection	$m(\tilde{g}) = 1400 \text{ GeV}$, $m(\tilde{\chi}_1^0) = 1000 \text{ GeV}$	$m(\tilde{g}) = 1800 \text{ GeV}$, $m(\tilde{\chi}_1^0) = 1000 \text{ GeV}$	$m(\tilde{g}) = 2200 \text{ GeV}$, $m(\tilde{\chi}_1^0) = 600 \text{ GeV}$
Generated MC events		60000	60000	50000
Common Requirements	Pre-selection, $E_T^{\text{miss}} > 300 \text{ GeV}$, $p_T(\text{jet}_1) > 200 \text{ GeV}$, $m_{\text{eff}} > 800 \text{ GeV}$ jet multiplicity ≥ 2 Cleaning Cuts	2562 2562 2532	467 467 461	57.6 57.6 56.8
SR4j-1000	jet multiplicity ≥ 4 $\Delta\phi(\text{jet}_{1,2,(3)}, \mathbf{p}_T^{\text{miss}})_{\text{min}} > 0.4$ $\Delta\phi(\text{jet}_{i>3}, \mathbf{p}_T^{\text{miss}})_{\text{min}} > 0.2$ $p_T(\text{jet}_4) > 100 \text{ GeV}$ $ \eta(j_{1,2,3,4}) < 2.0$ Aplanarity > 0.04 $E_T^{\text{miss}}/\sqrt{H_T} > 16 \text{ GeV}^{1/2}$ $m_{\text{eff}} > 1000 \text{ GeV}$	1931 1718 1583 661 574 429 149 149	410 357 322 234 214 159 82.7 82.7	53.5 44.7 39.8 35.3 32.1 22.3 13.9 13.9
SR4j-2200	jet multiplicity ≥ 4 $\Delta\phi(\text{jet}_{1,2,(3)}, \mathbf{p}_T^{\text{miss}})_{\text{min}} > 0.4$ $\Delta\phi(\text{jet}_{i>3}, \mathbf{p}_T^{\text{miss}})_{\text{min}} > 0.2$ $p_T(\text{jet}_4) > 100 \text{ GeV}$ $ \eta(j_{1,2,3,4}) < 2.0$ Aplanarity > 0.04 $E_T^{\text{miss}}/\sqrt{H_T} > 16 \text{ GeV}^{1/2}$ $m_{\text{eff}} > 2200 \text{ GeV}$	1931 1718 1583 661 574 429 149 13.7	410 357 322 234 214 159 82.7 34.9	53.5 44.7 39.8 35.3 32.1 22.3 13.9 13.6
SR4j-3400	jet multiplicity ≥ 4 $\Delta\phi(\text{jet}_{1,2,(3)}, \mathbf{p}_T^{\text{miss}})_{\text{min}} > 0.4$ $\Delta\phi(\text{jet}_{i>3}, \mathbf{p}_T^{\text{miss}})_{\text{min}} > 0.2$ $p_T(\text{jet}_4) > 100 \text{ GeV}$ $ \eta(j_{1,2,3,4}) < 2.0$ Aplanarity > 0.04 $E_T^{\text{miss}}/\sqrt{H_T} > 10 \text{ GeV}^{1/2}$ $m_{\text{eff}} > 3400 \text{ GeV}$	1931 1718 1583 661 574 429 398 0.279	410 357 322 234 214 159 142 1.43	53.5 44.7 39.8 35.3 32.1 22.3 19.6 8.04

Table 17: Cut-flow for model-independent search regions targeting gluinos for GG direct model points. Expected yields are normalized to a luminosity of 139 fb^{-1} .

	Selection	$m(\tilde{g}) = 800 \text{ GeV}$, $m(\tilde{\chi}_1^\pm) = 600 \text{ GeV}$, $m(\tilde{\chi}_1^0) = 400 \text{ GeV}$	$m(\tilde{g}) = 1400 \text{ GeV}$, $m(\tilde{\chi}_1^\pm) = 1100 \text{ GeV}$, $m(\tilde{\chi}_1^0) = 800 \text{ GeV}$	$m(\tilde{g}) = 2000 \text{ GeV}$, $m(\tilde{\chi}_1^\pm) = 1500 \text{ GeV}$, $m(\tilde{\chi}_1^0) = 1000 \text{ GeV}$	$m(\tilde{g}) = 2200 \text{ GeV}$, $m(\tilde{\chi}_1^\pm) = 1200 \text{ GeV}$, $m(\tilde{\chi}_1^0) = 200 \text{ GeV}$
Generated MC events		30000	30000	30000	30000
Common Requirements	Pre-selection, $E_T^{\text{miss}} > 300 \text{ GeV}$, $p_T(\text{jet}_1) > 200 \text{ GeV}$, $m_{\text{eff}} > 800 \text{ GeV}$	6101	1160	64.3	25.4
	jet multiplicity ≥ 2	6101	1160	64.3	25.4
	Cleaning Cuts	6039	1147	63.5	25.1
SR5j-1600	jet multiplicity ≥ 5	3513	1022	60.2	24.4
	$\Delta\phi(\text{jet}_{1,2,(3)}, \mathbf{p}_T^{\text{miss}})_{\text{min}} > 0.4$	2985	895	52.0	20.4
	$\Delta\phi(\text{jet}_{i>3}, \mathbf{p}_T^{\text{miss}})_{\text{min}} > 0.2$	2669	783	43.6	16.5
	$p_T(\text{jet}_1) > 600 \text{ GeV}$	240	46.2	10.7	13.1
	$E_T^{\text{miss}}/\sqrt{H_T} > 16 \text{ GeV}^{1/2}$	68.4	18.6	4.86	6.38
	$m_{\text{eff}} > 1600 \text{ GeV}$	68.4	18.4	4.86	6.38
SR6j-1000	jet multiplicity ≥ 6	1752	798	50.7	21.7
	$\Delta\phi(\text{jet}_{1,2,(3)}, \mathbf{p}_T^{\text{miss}})_{\text{min}} > 0.4$	1448	700	43.6	18.1
	$\Delta\phi(\text{jet}_{i>3}, \mathbf{p}_T^{\text{miss}})_{\text{min}} > 0.2$	1252	600	35.9	14.4
	$p_T(\text{jet}_6) > 75 \text{ GeV}$	388	313	25.7	12.3
	$ \eta(j_{1,2,3,4,5,6}) < 2.0$	250	260	22.6	10.5
	Aplanarity > 0.08	123	171	16.0	7.28
	$E_T^{\text{miss}}/\sqrt{H_T} > 16 \text{ GeV}^{1/2}$	10.4	42.8	6.91	3.58
	$m_{\text{eff}} > 1000 \text{ GeV}$	10.4	42.8	6.91	3.58
SR6j-2200	jet multiplicity ≥ 6	1752	798	50.7	21.7
	$\Delta\phi(\text{jet}_{1,2,(3)}, \mathbf{p}_T^{\text{miss}})_{\text{min}} > 0.4$	1448	700	43.6	18.1
	$\Delta\phi(\text{jet}_{i>3}, \mathbf{p}_T^{\text{miss}})_{\text{min}} > 0.2$	1252	600	35.9	14.4
	$p_T(\text{jet}_6) > 75 \text{ GeV}$	388	313	25.7	12.3
	$ \eta(j_{1,2,3,4,5,6}) < 2.0$	250	260	22.6	10.5
	Aplanarity > 0.08	123	171	16.0	7.28
	$E_T^{\text{miss}}/\sqrt{H_T} > 16 \text{ GeV}^{1/2}$	10.4	42.8	6.91	3.58
	$m_{\text{eff}} > 2200 \text{ GeV}$	3.31	4.96	4.87	3.57
SR6j-3400	jet multiplicity ≥ 6	1752	798	50.7	21.7
	$\Delta\phi(\text{jet}_{1,2,(3)}, \mathbf{p}_T^{\text{miss}})_{\text{min}} > 0.4$	1448	700	43.6	18.1
	$\Delta\phi(\text{jet}_{i>3}, \mathbf{p}_T^{\text{miss}})_{\text{min}} > 0.2$	1252	600	35.9	14.4
	$p_T(\text{jet}_6) > 75 \text{ GeV}$	388	313	25.7	12.3
	$ \eta(j_{1,2,3,4,5,6}) < 2.0$	250	260	22.6	10.5
	Aplanarity > 0.08	123	171	16.0	7.28
	$E_T^{\text{miss}}/\sqrt{H_T} > 10 \text{ GeV}^{1/2}$	84.6	143	13.5	6.03
	$m_{\text{eff}} > 3400 \text{ GeV}$	0.000	0.152	0.260	3.56

Table 18: Cut-flow for model-independent search regions targeting squarks and gluinos in models with one-step decays. Expected yields are normalized to a luminosity of 139 fb^{-1} .

References

- [1] Y. A. Gol'fand and E. P. Likhtman, *Extension of the Algebra of Poincare Group Generators and Violation of p Invariance*, JETP Lett. **13** (1971) 452, Pisma Zh. Eksp. Teor. Fiz. (cit. on p. 2).
- [2] D. V. Volkov and V. P. Akulov, *Is the Neutrino a Goldstone Particle?*, Phys. Lett. B **46** (1973) 109 (cit. on p. 2).
- [3] J. Wess and B. Zumino, *Supergauge Transformations in Four-Dimensions*, Nucl. Phys. B **70** (1974) 39 (cit. on p. 2).
- [4] J. Wess and B. Zumino, *Supergauge Invariant Extension of Quantum Electrodynamics*, Nucl. Phys. B **78** (1974) 1 (cit. on p. 2).
- [5] S. Ferrara and B. Zumino, *Supergauge Invariant Yang-Mills Theories*, Nucl. Phys. B **79** (1974) 413 (cit. on p. 2).
- [6] A. Salam and J. A. Strathdee, *Supersymmetry and Nonabelian Gauges*, Phys. Lett. B **51** (1974) 353 (cit. on p. 2).
- [7] G. R. Farrar and P. Fayet, *Phenomenology of the Production, Decay, and Detection of New Hadronic States Associated with Supersymmetry*, Phys. Lett. B **76** (1978) 575 (cit. on p. 2).
- [8] H. Goldberg, *Constraint on the Photino Mass from Cosmology*, Phys. Rev. Lett. **50** (1983) 1419 (cit. on p. 2).
- [9] J. R. Ellis, J. S. Hagelin, D. V. Nanopoulos, K. A. Olive and M. Srednicki, *Supersymmetric Relics from the Big Bang*, Nucl. Phys. B **238** (1984) 453 (cit. on p. 2).
- [10] L. Evans and P. Bryant, *LHC Machine*, JINST **3** (2008) S08001 (cit. on p. 2).
- [11] P. Fayet, *Supersymmetry and Weak, Electromagnetic and Strong Interactions*, Phys. Lett. B **64** (1976) 159 (cit. on p. 2).
- [12] P. Fayet, *Spontaneously Broken Supersymmetric Theories of Weak, Electromagnetic and Strong Interactions*, Phys. Lett. B **69** (1977) 489 (cit. on p. 2).
- [13] ATLAS Collaboration, *Search for squarks and gluinos in final states with jets and missing transverse momentum using 36 fb^{-1} of $\sqrt{s} = 13\text{ TeV}$ pp collision data with the ATLAS detector*, Phys. Rev. D **97** (2018) 112001, arXiv: [1712.02332 \[hep-ex\]](https://arxiv.org/abs/1712.02332) (cit. on pp. 2, 11, 30–34).
- [14] P. Speckmayer, A. Höcker, J. Stelzer and H. Voss, *The toolkit for multivariate data analysis, TMVA 4*, Journal of Physics: Conference Series **219** (2010) 032057 (cit. on p. 2).
- [15] CMS Collaboration, *A search for new phenomena in pp collisions at $\sqrt{s} = 13\text{ TeV}$ in final states with missing transverse momentum and at least one jet using the α_T variable*, Eur. Phys. J. C **77** (2017) 294, arXiv: [1611.00338 \[hep-ex\]](https://arxiv.org/abs/1611.00338) (cit. on p. 2).
- [16] CMS Collaboration, *Inclusive search for supersymmetry using razor variables in pp collisions at $\sqrt{s} = 13\text{ TeV}$* , Phys. Rev. D **95** (2017) 012003, arXiv: [1609.07658 \[hep-ex\]](https://arxiv.org/abs/1609.07658) (cit. on p. 2).
- [17] CMS Collaboration, *Search for new physics with the MT2 variable in all-jets final states produced in pp collisions at $\sqrt{s} = 13\text{ TeV}$* , JHEP **10** (2016) 006, arXiv: [1603.04053 \[hep-ex\]](https://arxiv.org/abs/1603.04053) (cit. on p. 2).
- [18] CMS Collaboration, *Search for natural and split supersymmetry in proton-proton collisions at $\sqrt{s} = 13\text{ TeV}$ in final states with jets and missing transverse momentum*, JHEP **05** (2018) 025, arXiv: [1802.02110 \[hep-ex\]](https://arxiv.org/abs/1802.02110) (cit. on p. 2).

[19] CMS Collaboration, *Search for new phenomena with the M_{T2} variable in the all-hadronic final state produced in proton-proton collisions at $\sqrt{s} = 13$ TeV*, *Eur. Phys. J. C* **77** (2017) 710, arXiv: [1705.04650 \[hep-ex\]](https://arxiv.org/abs/1705.04650) (cit. on p. 2).

[20] CMS Collaboration, *Search for supersymmetry in multijet events with missing transverse momentum in proton-proton collisions at 13 TeV*, *Phys. Rev. D* **96** (2017) 032003, arXiv: [1704.07781 \[hep-ex\]](https://arxiv.org/abs/1704.07781) (cit. on p. 2).

[21] ATLAS Collaboration, *Search for squarks and gluinos in events with an isolated lepton, jets, and missing transverse momentum at $\sqrt{s} = 13$ TeV with the ATLAS detector*, *Phys. Rev. D* **96** (2017) 112010, arXiv: [1708.08232 \[hep-ex\]](https://arxiv.org/abs/1708.08232) (cit. on p. 2).

[22] J. Alwall, M. Le, M. Lisanti and J. G. Wacker, *Searching for Directly Decaying Gluinos at the Tevatron*, *Phys. Lett. B* **666** (2008) 34, arXiv: [0803.0019 \[hep-ph\]](https://arxiv.org/abs/0803.0019) (cit. on p. 2).

[23] J. Alwall, P. Schuster and N. Toro, *Simplified Models for a First Characterization of New Physics at the LHC*, *Phys. Rev. D* **79** (2009) 075020, arXiv: [0810.3921 \[hep-ph\]](https://arxiv.org/abs/0810.3921) (cit. on p. 2).

[24] D. Alves et al., *Simplified Models for LHC New Physics Searches*, *J. Phys. G* **39** (2012) 105005, arXiv: [1105.2838 \[hep-ph\]](https://arxiv.org/abs/1105.2838) (cit. on p. 2).

[25] ATLAS Collaboration, *The ATLAS Experiment at the CERN Large Hadron Collider*, *JINST* **3** (2008) S08003 (cit. on p. 3).

[26] ATLAS Collaboration, *ATLAS Insertable B-Layer Technical Design Report*, ATLAS-TDR-19 (2010), URL: <https://cdsweb.cern.ch/record/1291633>, *ATLAS Insertable B-Layer Technical Design Report Addendum*, ATLAS-TDR-19-ADD-1, 2012, URL: <https://cds.cern.ch/record/1451888> (cit. on p. 3).

[27] B. Abbott et al., *Production and Integration of the ATLAS Insertable B-Layer*, *JINST* **13** (2018) T05008, arXiv: [1803.00844 \[physics.ins-det\]](https://arxiv.org/abs/1803.00844) (cit. on p. 3).

[28] ATLAS Collaboration, *Performance of the ATLAS Trigger System in 2015*, *Eur. Phys. J. C* **77** (2017) 317, arXiv: [1611.09661 \[hep-ex\]](https://arxiv.org/abs/1611.09661) (cit. on p. 3).

[29] ATLAS Collaboration, *Luminosity determination in pp collisions at $\sqrt{s} = 13$ TeV using the ATLAS detector at the LHC*, ATLAS-CONF-2019-021, 2019, URL: <https://cds.cern.ch/record/2677054> (cit. on p. 3).

[30] G. Avoni et al., *The new LUCID-2 detector for luminosity measurement and monitoring in ATLAS*, *JINST* **13** (2018) P07017 (cit. on p. 3).

[31] A. Djouadi, M. Muhlleitner and M. Spira, *Decays of supersymmetric particles: The Program SUSY-HIT (SUspect-SdecaY-Hdecay-Interface)*, *Acta Phys. Polon. B* **38** (2007) 635, arXiv: [hep-ph/0609292 \[hep-ph\]](https://arxiv.org/abs/hep-ph/0609292) (cit. on p. 4).

[32] J. Alwall et al., *The automated computation of tree-level and next-to-leading order differential cross sections, and their matching to parton shower simulations*, *JHEP* **07** (2014) 079, arXiv: [1405.0301 \[hep-ph\]](https://arxiv.org/abs/1405.0301) (cit. on pp. 4, 5).

[33] T. Sjöstrand et al., *An Introduction to PYTHIA 8.2*, *Comput. Phys. Commun.* **191** (2015) 159, arXiv: [1410.3012 \[hep-ph\]](https://arxiv.org/abs/1410.3012) (cit. on pp. 4, 5).

[34] L. Lönnblad and S. Prestel, *Matching Tree-Level Matrix Elements with Interleaved Showers*, *JHEP* **03** (2012) 019, arXiv: [1109.4829 \[hep-ph\]](https://arxiv.org/abs/1109.4829) (cit. on p. 4).

[35] ATLAS Collaboration, *Summary of ATLAS Pythia 8 tunes*, ATL-PHYS-PUB-2012-003 (2012), URL: <https://cdsweb.cern.ch/record/1474107> (cit. on pp. 4, 5).

[36] R. D. Ball et al., *Parton distributions with LHC data*, *Nucl. Phys. B* **867** (2013) 244, arXiv: [1207.1303 \[hep-ph\]](https://arxiv.org/abs/1207.1303) (cit. on pp. 4, 5).

[37] W. Beenakker, C. Borschensky, M. Krämer, A. Kulesza and E. Laenen, *NNLL-fast: predictions for coloured supersymmetric particle production at the LHC with threshold and Coulomb resummation*, *JHEP* **12** (2016) 133, arXiv: [1607.07741 \[hep-ph\]](https://arxiv.org/abs/1607.07741) (cit. on p. 4).

[38] W. Beenakker et al., *NNLL resummation for squark and gluino production at the LHC*, *JHEP* **12** (2014) 023, arXiv: [1404.3134 \[hep-ph\]](https://arxiv.org/abs/1404.3134) (cit. on p. 4).

[39] W. Beenakker et al., *Towards NNLL resummation: hard matching coefficients for squark and gluino hadroproduction*, *JHEP* **10** (2013) 120, arXiv: [1304.6354 \[hep-ph\]](https://arxiv.org/abs/1304.6354) (cit. on p. 4).

[40] W. Beenakker et al., *NNLL resummation for squark-antisquark pair production at the LHC*, *JHEP* **01** (2012) 076, arXiv: [1110.2446 \[hep-ph\]](https://arxiv.org/abs/1110.2446) (cit. on p. 4).

[41] W. Beenakker et al., *Soft-gluon resummation for squark and gluino hadroproduction*, *JHEP* **12** (2009) 041, arXiv: [0909.4418 \[hep-ph\]](https://arxiv.org/abs/0909.4418) (cit. on p. 4).

[42] A. Kulesza and L. Motyka, *Soft gluon resummation for the production of gluino-gluino and squark-antisquark pairs at the LHC*, *Phys. Rev. D* **80** (2009) 095004, arXiv: [0905.4749 \[hep-ph\]](https://arxiv.org/abs/0905.4749) (cit. on p. 4).

[43] A. Kulesza and L. Motyka, *Threshold resummation for squark-antisquark and gluino-pair production at the LHC*, *Phys. Rev. Lett.* **102** (2009) 111802, arXiv: [0807.2405 \[hep-ph\]](https://arxiv.org/abs/0807.2405) (cit. on p. 4).

[44] W. Beenakker et al., *Squark and gluino production at hadron colliders*, *Nucl. Phys. B* **492** (1997) 51, arXiv: [hep-ph/9610490](https://arxiv.org/abs/hep-ph/9610490) (cit. on p. 4).

[45] J. Butterworth et al., *PDF4LHC recommendations for LHC Run II*, *J. Phys. G* **43** (2016) 023001, arXiv: [1510.03865 \[hep-ph\]](https://arxiv.org/abs/1510.03865) (cit. on p. 4).

[46] T. Gleisberg et al., *Event generation with SHERPA 1.1*, *JHEP* **02** (2009) 007, arXiv: [0811.4622 \[hep-ph\]](https://arxiv.org/abs/0811.4622) (cit. on p. 5).

[47] R. Gavin, Y. Li, F. Petriello and S. Quackenbush, *FEWZ 2.0: A code for hadronic Z production at next-to-next-to-leading order*, *Comput. Phys. Commun.* **182** (2011) 2388, arXiv: [1011.3540 \[hep-ph\]](https://arxiv.org/abs/1011.3540) (cit. on p. 5).

[48] R. D. Ball et al., *Parton distributions for the LHC Run II*, *JHEP* **04** (2015) 040, arXiv: [1410.8849 \[hep-ph\]](https://arxiv.org/abs/1410.8849) (cit. on p. 5).

[49] S. Höche, F. Krauss, S. Schumann and F. Siegert, *QCD matrix elements and truncated showers*, *JHEP* **05** (2009) 053, arXiv: [0903.1219 \[hep-ph\]](https://arxiv.org/abs/0903.1219) (cit. on p. 5).

[50] S. Alioli, P. Nason, C. Oleari and E. Re, *A general framework for implementing NLO calculations in shower Monte Carlo programs: the POWHEG BOX*, *JHEP* **06** (2010) 043, arXiv: [1002.2581 \[hep-ph\]](https://arxiv.org/abs/1002.2581) (cit. on p. 5).

[51] M. Czakon, P. Fiedler and A. Mitov, *Total Top-Quark Pair-Production Cross Section at Hadron Colliders Through $O(\alpha_S^4)$* , *Phys. Rev. Lett.* **110** (2013) 252004, arXiv: [1303.6254 \[hep-ph\]](https://arxiv.org/abs/1303.6254) (cit. on p. 5).

[52] M. Czakon and A. Mitov, *Top++: A Program for the Calculation of the Top-Pair Cross-Section at Hadron Colliders*, *Comput. Phys. Commun.* **185** (2014) 2930, arXiv: [1112.5675 \[hep-ph\]](https://arxiv.org/abs/1112.5675) (cit. on p. 5).

[53] ATLAS Collaboration, *ATLAS Pythia 8 tunes to 7 TeV data*, ATL-PHYS-PUB-2014-021, 2014, URL: <https://cds.cern.ch/record/1966419> (cit. on p. 5).

[54] N. Kidonakis, *Two-loop soft anomalous dimensions for single top quark associated production with a W- or H-*, *Phys. Rev. D* **82** (2010) 054018, arXiv: [1005.4451 \[hep-ph\]](https://arxiv.org/abs/1005.4451) (cit. on p. 5).

[55] N. Kidonakis, *Next-to-next-to-leading-order collinear and soft gluon corrections for t-channel single top quark production*, *Phys. Rev. D* **83** (2011) 091503, arXiv: [1103.2792 \[hep-ph\]](https://arxiv.org/abs/1103.2792) (cit. on p. 5).

[56] M. Aliev et al., *HATHOR: HArdonic Top and Heavy quarks crOss section calculatoR*, *Comput. Phys. Commun.* **182** (2011) 1034, arXiv: [1007.1327 \[hep-ph\]](https://arxiv.org/abs/1007.1327) (cit. on p. 5).

[57] P. Kant et al., *HatHor for single top-quark production: Updated predictions and uncertainty estimates for single top-quark production in hadronic collisions*, *Comput. Phys. Commun.* **191** (2015) 74, arXiv: [1406.4403 \[hep-ph\]](https://arxiv.org/abs/1406.4403) (cit. on p. 5).

[58] A. Lazopoulos, T. McElmurry, K. Melnikov and F. Petriello, *Next-to-leading order QCD corrections to $t\bar{t}Z$ production at the LHC*, *Phys. Lett. B* **666** (2008) 62, arXiv: [0804.2220 \[hep-ph\]](https://arxiv.org/abs/0804.2220) (cit. on p. 5).

[59] J. M. Campbell and R. K. Ellis, *$t\bar{t}W^\pm$ production and decay at NLO*, *JHEP* **07** (2012) 052, arXiv: [1204.5678 \[hep-ph\]](https://arxiv.org/abs/1204.5678) (cit. on p. 5).

[60] ATLAS Collaboration, *The ATLAS Simulation Infrastructure*, *Eur. Phys. J. C* **70** (2010) 823, arXiv: [1005.4568 \[physics.ins-det\]](https://arxiv.org/abs/1005.4568) (cit. on p. 4).

[61] S. Agostinelli et al., *GEANT4: A simulation toolkit*, *Nucl. Instrum. Meth. A* **506** (2003) 250 (cit. on p. 4).

[62] D. J. Lange, *The EvtGen particle decay simulation package*, *Nucl. Instrum. Meth. A* **462** (2001) 152 (cit. on p. 4).

[63] M. Cacciari, G. P. Salam and G. Soyez, *The anti- k_t jet clustering algorithm*, *JHEP* **04** (2008) 063, arXiv: [0802.1189 \[hep-ph\]](https://arxiv.org/abs/0802.1189) (cit. on p. 6).

[64] M. Cacciari, G. P. Salam and G. Soyez, *FastJet User Manual*, *Eur. Phys. J. C* **72** (2012) 1896, arXiv: [1111.6097 \[hep-ph\]](https://arxiv.org/abs/1111.6097) (cit. on p. 6).

[65] ATLAS Collaboration, *Topological cell clustering in the ATLAS calorimeters and its performance in LHC Run 1*, *Eur. Phys. J. C* **77** (2017) 490, arXiv: [1603.02934 \[hep-ex\]](https://arxiv.org/abs/1603.02934) (cit. on p. 6).

[66] M. Cacciari and G. P. Salam, *Pileup subtraction using jet areas*, *Phys. Lett. B* **659** (2008) 119, arXiv: [0707.1378 \[hep-ph\]](https://arxiv.org/abs/0707.1378) (cit. on p. 6).

[67] ATLAS Collaboration, *Performance of pile-up mitigation techniques for jets in pp collisions at $\sqrt{s} = 8$ TeV using the ATLAS detector*, *Eur. Phys. J. C* **76** (2016) 581, arXiv: [1510.03823 \[hep-ex\]](https://arxiv.org/abs/1510.03823) (cit. on p. 6).

[68] ATLAS Collaboration, *Jet energy scale measurements and their systematic uncertainties in proton-proton collisions at $\sqrt{s} = 13$ TeV with the ATLAS detector*, *Phys. Rev. D* **96** (2017) 072002, arXiv: [1703.09665 \[hep-ex\]](https://arxiv.org/abs/1703.09665) (cit. on p. 6).

[69] ATLAS Collaboration, *Optimisation of the ATLAS b-tagging performance for the 2016 LHC Run*, ATL-PHYS-PUB-2016-012 (2016), URL: <https://cds.cern.ch/record/2160731> (cit. on p. 6).

[70] ATLAS Collaboration, *Performance of b-Jet Identification in the ATLAS Experiment*, *JINST* **11** (2016) P04008, arXiv: [1512.01094 \[hep-ex\]](https://arxiv.org/abs/1512.01094) (cit. on p. 6).

[71] ATLAS Collaboration, *Characterisation and mitigation of beam-induced backgrounds observed in the ATLAS detector during the 2011 proton-proton run*, *JINST* **8** (2013) P07004, arXiv: [1303.0223 \[hep-ex\]](https://arxiv.org/abs/1303.0223) (cit. on p. 6).

[72] ATLAS Collaboration, *Tagging and suppression of pileup jets with the ATLAS detector*, ATLAS-CONF-2014-018 (2014), URL: <https://cds.cern.ch/record/1700870> (cit. on p. 6).

[73] ATLAS Collaboration, *Muon reconstruction performance of the ATLAS detector in proton–proton collision data at $\sqrt{s} = 13$ TeV*, *Eur. Phys. J. C* **76** (2016) 292, arXiv: [1603.05598 \[hep-ex\]](https://arxiv.org/abs/1603.05598) (cit. on p. 6).

[74] ATLAS Collaboration, *Electron reconstruction and identification in the ATLAS experiment using the 2015 and 2016 LHC proton–proton collision data at $\sqrt{s} = 13$ TeV*, Submitted to: *Eur. Phys. J.* (2019), arXiv: [1902.04655 \[physics.ins-det\]](https://arxiv.org/abs/1902.04655) (cit. on p. 6).

[75] ATLAS Collaboration, *Electron efficiency measurements with the ATLAS detector using 2012 LHC proton–proton collision data*, *Eur. Phys. J. C* **77** (2017) 195, arXiv: [1612.01456 \[hep-ex\]](https://arxiv.org/abs/1612.01456) (cit. on p. 6).

[76] ATLAS Collaboration, *Measurement of the photon identification efficiencies with the ATLAS detector using LHC Run-1 data*, *Eur. Phys. J. C* **76** (2016) 666, arXiv: [1606.01813 \[hep-ex\]](https://arxiv.org/abs/1606.01813) (cit. on p. 7).

[77] ATLAS Collaboration, *Performance of missing transverse momentum reconstruction with the ATLAS detector using proton–proton collisions at $\sqrt{s} = 13$ TeV*, *Eur. Phys. J. C* **78** (2018) 903, arXiv: [1802.08168 \[hep-ex\]](https://arxiv.org/abs/1802.08168) (cit. on pp. 7, 21).

[78] ATLAS Collaboration, *E_T^{miss} performance in the ATLAS detector using 2015–2016 LHC pp collisions*, ATLAS-CONF-2018-023, 2018, URL: <https://cds.cern.ch/record/2625233> (cit. on p. 7).

[79] J. D. Bjorken and S. J. Brodsky, *Statistical Model for Electron-Positron Annihilation into Hadrons*, *Phys. Rev. D* **1** (5 1970) 1416, URL: <https://link.aps.org/doi/10.1103/PhysRevD.1.1416> (cit. on p. 9).

[80] ATLAS Collaboration, *Search for squarks and gluinos with the ATLAS detector in final states with jets and missing transverse momentum using 4.7 fb^{-1} of $\sqrt{s} = 7$ TeV proton–proton collision data*, *Phys. Rev. D* **87** (2013) 012008, arXiv: [1208.0949 \[hep-ex\]](https://arxiv.org/abs/1208.0949) (cit. on pp. 13, 14).

[81] M. Baak, G. Besjes, D. Cote, A. Koutsman, J. Lorenz et al., *HistFitter software framework for statistical data analysis*, *Eur. Phys. J. C* **75** (2015) 153, arXiv: [1410.1280 \[hep-ex\]](https://arxiv.org/abs/1410.1280) (cit. on pp. 14, 23).

[82] ATLAS Collaboration, *Improvements in $t\bar{t}$ modelling using NLO+PS Monte Carlo generators for Run 2*, ATL-PHYS-PUB-2018-009, 2018, URL: <https://cds.cern.ch/record/2630327> (cit. on p. 14).

[83] R. D. Cousins, J. T. Linnemann and J. Tucker, *Evaluation of three methods for calculating statistical significance when incorporating a systematic uncertainty into a test of the background-only hypothesis for a Poisson process*, *Nucl. Instrum. Meth. A* **595** (2008) 480, arXiv: [physics/0702156 \[physics.data-an\]](https://arxiv.org/abs/physics/0702156) (cit. on pp. 18–20, 29).

[84] ATLAS Collaboration, *Jet energy scale measurements and their systematic uncertainties in proton–proton collisions at $\sqrt{s} = 13$ TeV with the ATLAS detector*, *Phys. Rev. D* **96** (2017) 072002, arXiv: [1703.09665 \[hep-ex\]](https://arxiv.org/abs/1703.09665) (cit. on p. 21).

[85] ATLAS Collaboration, *Jet Calibration and Systematic Uncertainties for Jets Reconstructed in the ATLAS Detector at $\sqrt{s} = 13$ TeV*, ATL-PHYS-PUB-2015-015, 2015, URL: <https://cds.cern.ch/record/2037613> (cit. on p. 21).

[86] J. Bellm et al., *Herwig 7.0/Herwig++ 3.0 release note*, *Eur. Phys. J. C* **76** (2016) 196, arXiv: [1512.01178 \[hep-ph\]](https://arxiv.org/abs/1512.01178) (cit. on p. 22).

- [87] A. L. Read, *Presentation of Search Results: The $CL(s)$ Technique*, *J. Phys. G* **28** (2002) 2693 (cit. on p. 23).
- [88] G. Cowan, K. Cranmer, E. Gross and O. Vitells, *Asymptotic formulae for likelihood-based tests of new physics*, *Eur. Phys. J. C* **71** (2011) 1554, arXiv: [1007.1727 \[physics.data-an\]](https://arxiv.org/abs/1007.1727) (cit. on p. 23).